The Astrophysical Journal, 827:51 (16pp), 2016 August 10 doi:10.3847/0004-637X/827/1/51

OBSERVATION AND CONFIRMATION OF SIX STRONG-LENSING SYSTEMS IN THE DARK ENERGY SURVEY SCIENCE VERIFICATION DATA*

B. Nord[1], E. Buckley-Geer[1], H. Lin[1], H. T. Diehl[1], J. Helsby[2], N. Kuropatkin[1], A. Amara[3], T. Collett[4], S. Allam[1], G. B. Caminha[5,6], C. De Bom[5,7], S. Desai[8,9], H. Dúmet-Montoya[10], M. Elidaiana da S. Pereira[5], D. A. Finley[1], B. Flaugher[1], C. Furlanetto[11], H. Gaitsch[1], M. Gill[12], K. W. Merritt[1], A. More[13], D. Tucker[1], A. Saro[14], E. S. Rykoff[12,15], E. Rozo[16], S. Birrer[3], F. B. Abdalla[17,18], A. Agnello[19], M. Auger[20], R. J. Brunner[21,22], M. Carrasco Kind[21,22], F. J. Castander[23], C. E. Cunha[15], L. N. da Costa[24,25], R. J. Foley[21,26], D. W. Gerdes[27], K. Glazebrook[28], J. Gschwend[24,25], W. Hartley[3], R. Kessler[2], D. Lagattuta[29], G. Lewis[30], M. A. G. Maia[24,25], M. Makler[5], F. Menanteau[21,22], A. Niernberg[31], D. Scolnic[2], J. D. Vieira[21,22,26], R. Gramillano[21], T. M. C. Abbott[32], M. Banerji[20,33], A. Benoit-Lévy[17,34,35], D. Brooks[17], D. L. Burke[12,15], D. Capozzi[4], A. Carnero Rosell[24,25], J. Carretero[23,36], C. B. D'Andrea[4,37], J. P. Dietrich[8,9], P. Doel[17], A. E. Evrard[27,38], J. Frieman[1,2], E. Gaztanaga[23], D. Gruen[39,40], K. Honscheid[31,41], D. J. James[32], K. Kuehn[42], T. S. Li[43], M. Lima[24,44], J. L. Marshall[43], P. Martini[31,45], P. Melchior[31,41,46], R. Miquel[36,47], E. Neilsen[1], R. C. Nichol[4], R. Ogando[24,25], A. A. Plazas[48], A. K. Romer[49], M. Sako[50], E. Sanchez[51], V. Scarpine[1], M. Schubnell[27], I. Sevilla-Noarbe[21,51], R. C. Smith[32], M. Soares-Santos[1], F. Sobreira[1,24], E. Suchyta[50], M. E. C. Swanson[22], G. Tarle[27], J. Thaler[26], A. R. Walker[32], W. Wester[1], and Y. Zhang[27]

(The DES Collaboration)

[1] Fermi National Accelerator Laboratory, P.O. Box 500, Batavia, IL 60510, USA; nord@fnal.gov
[2] Kavli Institute for Cosmological Physics, University of Chicago, Chicago, IL 60637, USA
[3] Department of Physics, ETH Zurich, Wolfgang-Pauli-Strasse 16, CH-8093 Zurich, Switzerland
[4] Institute of Cosmology & Gravitation, University of Portsmouth, Portsmouth, PO1 3FX, UK
[5] ICRA, Centro Brasileiro de Pesquisas Físicas, Rua Dr. Xavier Sigaud 150, CEP 22290-180, Rio de Janeiro, RJ, Brazil
[6] Dipartimento di Fisica e Scienze della Terra, Università degli Studi di Ferrara, Via Saragat 1, I-44122 Ferrara, Italy
[7] Centro Federal de Educação Tecnológica Celso Suckow da Fonseca, Rodovia Mário Covas, lote J2, quadra J, Cep 23810-000, Itaguaí, RJ, Brazil
[8] Excellence Cluster Universe, Boltzmannstrasse 2, D-85748 Garching, Germany
[9] Faculty of Physics, Ludwig-Maximilians University, Scheinerstrasse 1, D-81679 Munich, Germany
[10] Universidade Federal do Rio de Janeiro—Campus Macaé, Rua Aloísio Gomes da Silva, 50—Granja dos Cavaleiros, Cep: 27930-560, Macaé, RJ, Brazil
[11] University of Nottingham, School of Physics and Astronomy, Nottingham NG7 2RD, UK
[12] SLAC National Accelerator Laboratory, Menlo Park, CA 94025, USA
[13] Kavli IPMU (WPI), UTIAS, The University of Tokyo, Kashiwa, Chiba 277-8583, Japan
[14] Faculty of Physics, Ludwig-Maximilians-Universität, Scheinerstrasse 1, D-81679 Munich, Germany
[15] Kavli Institute for Particle Astrophysics & Cosmology, P.O. Box 2450, Stanford University, Stanford, CA 94305, USA
[16] Department of Physics, University of Arizona, Tucson, AZ 85721, USA
[17] Department of Physics & Astronomy, University College London, Gower Street, London, WC1E 6BT, UK
[18] Department of Physics and Electronics, Rhodes University, P.O. Box 94, Grahamstown, 6140, South Africa
[19] Department of Physics and Astronomy, PAB, 430 Portola Plaza, Box 951547, Los Angeles, CA 90095-1547, USA
[20] Institute of Astronomy, University of Cambridge, Madingley Road, Cambridge CB3 0HA, UK
[21] Department of Astronomy, University of Illinois, 1002 W. Green Street, Urbana, IL 61801, USA
[22] National Center for Supercomputing Applications, 1205 West Clark Street, Urbana, IL 61801, USA
[23] Institut de Ciències de l'Espai, IEEC-CSIC, Campus UAB, Carrer de Can Magrans, s/n, E-08193 Bellaterra, Barcelona, Spain
[24] Laboratório Interinstitucional de e-Astronomia—LIneA, Rua Gal. José Cristino 77, Rio de Janeiro, RJ 20921-400, Brazil
[25] Observatório Nacional, Rua Gal. José Cristino 77, Rio de Janeiro, RJ 20921-400, Brazil
[26] Department of Physics, University of Illinois, 1110 W. Green Street, Urbana, IL 61801, USA
[27] Department of Physics, University of Michigan, Ann Arbor, MI 48109, USA
[28] Centre for Astrophysics & Supercomputing, Swinburne University of Technology, Victoria 3122, Australia
[29] Centre de Recherche Astrophysique de Lyon, Université de Lyon, Université Lyon 1, CNRS, Observatoire de Lyon; 9 avenue Charles Andrè, F-69561 Saint-Genis Laval Cedex, France
[30] Sydney Institute for Astronomy, School of Physics A28, The University of Sydney, NSW 2006, Australia
[31] Center for Cosmology and Astro-Particle Physics, The Ohio State University, Columbus, OH 43210, USA
[32] Cerro Tololo Inter-American Observatory, National Optical Astronomy Observatory, Casilla 603, La Serena, Chile
[33] Kavli Institute for Cosmology, University of Cambridge, Madingley Road, Cambridge CB3 0HA, UK
[34] CNRS, UMR 7095, Institut d'Astrophysique de Paris, F-75014, Paris, France
[35] Sorbonne Universités, UPMC Univ Paris 06, UMR 7095, Institut d'Astrophysique de Paris, F-75014, Paris, France
[36] Institut de Física d'Altes Energies (IFAE), The Barcelona Institute of Science and Technology, Campus UAB, E-08193 Bellaterra (Barcelona) Spain
[37] School of Physics and Astronomy, University of Southampton, Southampton, SO17 1BJ, UK
[38] Department of Astronomy, University of Michigan, Ann Arbor, MI 48109, USA
[39] Max Planck Institute for Extraterrestrial Physics, Giessenbachstrasse, D-85748 Garching, Germany
[40] Universitäts-Sternwarte, Fakultät für Physik, Ludwig-Maximilians Universität München, Scheinerstrasse 1, D-81679 München, Germany
[41] Department of Physics, The Ohio State University, Columbus, OH 43210, USA
[42] Australian Astronomical Observatory, North Ryde, NSW 2113, Australia
[43] George P. and Cynthia Woods Mitchell Institute for Fundamental Physics and Astronomy, and Department of Physics and Astronomy, Texas A&M University, College Station, TX 77843, USA
[44] Departamento de Física Matemática, Instituto de Física, Universidade de São Paulo, CP 66318, CEP 05314-970, São Paulo, SP, Brazil
[45] Department of Astronomy, The Ohio State University, Columbus, OH 43210, USA
[46] Department of Astrophysical Sciences, Princeton University, Peyton Hall, Princeton, NJ 08544, USA
[47] Institució Catalana de Recerca i Estudis Avançats, E-08010 Barcelona, Spain

* This paper includes data gathered with the 6.5 m Magellan Telescopes located at Las Campanas Observatory, Chile.

[48] Jet Propulsion Laboratory, California Institute of Technology, 4800 Oak Grove Drive, Pasadena, CA 91109, USA
[49] Department of Physics and Astronomy, Pevensey Building, University of Sussex, Brighton, BN1 9QH, UK
[50] Department of Physics and Astronomy, University of Pennsylvania, Philadelphia, PA 19104, USA
[51] Centro de Investigaciones Energéticas, Medioambientales y Tecnológicas (CIEMAT), Madrid, Spain
Received 2015 December 5; revised 2016 April 19; accepted 2016 April 20; published 2016 August 5

ABSTRACT

We report the observation and confirmation of the first group- and cluster-scale strong gravitational lensing systems found in Dark Energy Survey data. Through visual inspection of data from the Science Verification season, we identified 53 candidate systems. We then obtained spectroscopic follow-up of 21 candidates using the Gemini Multi-object Spectrograph at the Gemini South telescope and the Inamori-Magellan Areal Camera and Spectrograph at the Magellan/Baade telescope. With this follow-up, we confirmed six candidates as gravitational lenses: three of the systems are newly discovered, and the remaining three were previously known. Of the 21 observed candidates, the remaining 15 either were not detected in spectroscopic observations, were observed and did not exhibit continuum emission (or spectral features), or were ruled out as lensing systems. The confirmed sample consists of one group-scale and five galaxy-cluster-scale lenses. The lensed sources range in redshift $z \sim 0.80$–3.2 and in i-band surface brightness $i_{\rm SB} \sim 23$–25 mag arcsec^{-2} ($2''$ aperture). For each of the six systems, we estimate the Einstein radius $\theta_{\rm E}$ and the enclosed mass $M_{\rm enc}$, which have ranges $\theta_{\rm E} \sim 5''$–$9''$ and $M_{\rm enc} \sim 8 \times 10^{12}$ to $6 \times 10^{13}\,M_{\odot}$, respectively.

Key words: cosmology: observations – galaxies: clusters: general – galaxies: distances and redshifts – gravitational lensing: strong – methods: observational – techniques: spectroscopic

1. INTRODUCTION

Strong gravitational lensing of galaxies and quasars provides opportunities to study cosmology, dark matter, dark energy, galactic structure, and galaxy evolution (Treu 2010). Strong lensing also provides a sample of galaxies—the lenses themselves—that are selected based on total mass, rather than luminosity or surface brightness (e.g., Reblinsky & Bartelmann 1999): the distortion of images by the lens depends only on the total lens mass and its spatial distribution.[52]

The majority of strong-lensing systems discovered in the past decade were found with a variety of techniques, mostly through dedicated investigations of existing data or through new dedicated surveys. Data from the Sloan Digital Sky Survey (York et al. 2000), for example, have been used by a number of groups to select lens candidates. The Optimal Line-of-Sight-lens Survey (Willis et al. 2006) discovered five galaxy-scale lenses. Investigating a sample of rich galaxy clusters, Hennawi et al. (2008) found 37 lenses of varying size and morphology. The Sloan Bright Arc Survey (SBAS; Allam et al. 2007; Kubik 2007; Diehl et al. 2009; Kubo et al. 2009, 2010; Lin et al. 2009; Wiesner et al. 2012) discovered 28 galaxy- and group-scale systems. The Sloan Lens ACS Survey group (Bolton et al. 2008) identified 137 lensing candidates, using both the spectroscopic and imaging catalogs. The CAmbridge Sloan Survey Of Wide ARcs in the skY (Belokurov et al. 2009) searched for wide-separation, galaxy-scale systems, uncovering 45 systems to date. Other searches, like the Strong Lensing Legacy Survey (SL2S; e.g., Cabanac et al. 2007; More et al. 2012), have yielded 127 lens candidates—spanning group to cluster scales—from $\sim$150 deg^2 of sky area in the Canada–France–Hawaii Telescope Legacy Survey (CFHTLS). Searches in the COSMOS field (Faure et al. 2008; Jackson 2008) have yielded 70 lens candidates.

Surveys in other bands have also proven successful. The Cosmic Lens All-Sky Survey[53] (CLASS; e.g., Browne et al. 2003; Myers et al. 2003; York et al. 2005) confirmed nearly 25 radio-loud galaxy-scale lensing systems. Several of them have multiply imaged sources, including the four-image system CLASS B2045+265 (Fassnacht et al. 1999) and the two-component wide-separation ($4\farcs56$) system CLASS B2108 +213 (McKean et al. 2005).

There is a history of targeting massive galaxy clusters to use as cosmic lenses for the study of high-redshift star-forming galaxies in the infrared (e.g., Smail et al. 1997; Egami et al. 2010; Swinbank et al. 2010). Recently, wide-field millimeter and submillimeter surveys have enabled the discovery of new populations of strong-lensing systems based on a simple flux-density selection (Blain 1996; Negrello et al. 2007) with near-100% completeness (Negrello et al. 2010; Vieira et al. 2010; Bussmann et al. 2013). These wide-field surveys, coupled with the recently commissioned Atacama Large Millimeter Array (ALMA), have opened a new window to star formation at high redshifts (e.g., Vieira et al. 2013; ALMA Partnership et al. 2015).

These investigations—from optical to millimeter wavebands —produced on the order of 1000 lensing candidates or confirmed lenses, spanning a range of arc sizes—from small arcs ($\theta_{\rm E} \sim 3''$) produced by single-galaxy lenses to giant arcs typically found in clusters ($\theta_{\rm E} \sim 10''$).

The Dark Energy Survey (DES[54]; Diehl et al. 2014; Flaugher et al. 2015)—a new, deep sky survey covering 5000 deg^2 of the Southern Galactic Cap in five optical filters (*grizY*)—is suitable for a systematic census of gravitational lenses. The wide-field survey will have a depth of $i \sim 24$ mag at 10σ detection threshold, and the 30 deg^2 supernova survey is spread over 10 fields—eight shallow and two deep. The primary instrument for DES is the newly assembled Dark Energy Camera (DECam), a wide-field (3 deg^2) CCD mosaic camera located on the Blanco 4 m telescope at the Cerro Tololo Inter-American Observatory in the Chilean Andes. The DES footprint is best observed

[52] This is not the case for strong-lensing systems with multiple lens planes spread out across the distance between the lens and source, but these cases are relatively rare.

[53] http://www.aoc.nrao.edu/~smyers/class.html
[54] www.darkenergysurvey.org

between August and mid-February. DES observes for ∼105 nights yr^{-1} and has completed 3 of the 5 yr of planned observations. The survey will produce the widest, deepest, and most uniform contiguous map in optical wavelengths of the southern sky, much of which has not been systematically surveyed—and not at such depth—until now. These features make DES suitable for finding many strong-lensing systems that span large ranges in redshift and Einstein radii. DES expects to uncover a large and diverse sample of strong gravitational lenses, which will provide for a rich science program.

One of the main objectives of the strong-lensing science program in DES is to derive constraints on dark energy. One of the two key components will be exploiting galaxy- and cluster-scale lenses that have multiple background sources at different redshifts. When there exist two lensed sources, one source will lie between the lens and the other, more distant source: these sources produce distinct Einstein radii. The ratio of the Einstein radii (and thus, a ratio of angular diameter distances) is independent of the Hubble constant and only weakly dependent on the lens mass distribution. Provided that the lensing mass can be well modeled, the ratio of distance ratios can help to constrain dark energy models (Gavazzi et al. 2008; Jullo et al. 2010; Collett et al. 2012; Collett & Auger 2014).

The second key component is to use strongly lensed quasars to measure cosmological parameters (e.g., H_0) by utilizing the time delays between multiple images (Refsdal 1964; Suyu et al. 2013; Birrer et al. 2015) of time-varying sources. We predict that the wide-field survey should contain about 120 lensed quasars brighter than $i = 21$ mag (Oguri & Marshall 2010), of which ∼20 would be high-information-content quadruple-image configurations. Through the STRong-lensing Insights into DES (STRIDES) program,[55] DES has discovered and confirmed two lensed quasars so far at $z \sim 1.6$ and ∼2.4 (Agnello et al. 2015). In addition, 30 deg^2 of deep imaging in the supernova fields, which have a high cadence, provides an opportunity to find lensed supernovae.

In addition to constraining cosmology, we will use a substantial cluster-scale lens sample to study dark matter mass profiles. Also, we expect to discover a large sample of sources at varying redshifts that will be valuable for studies of galaxy evolution.

In this paper, we report on the search for strong lens systems from the DES Science Verification (SV) data. We performed a visual inspection of the ∼250 deg^2 SV area, discovering a large number of candidates, which we then culled to 53 high-ranking candidates. We selected 24 for spectroscopic follow-up and were able to observe 21 of them. Of the sample we followed up, we focus on six systems that have compelling evidence (color, morphology, and spectroscopy) of strong gravitational lensing: three of these are newly identified, and three are already known from other surveys. We have spectroscopically confirmed these six systems (Figure 1) as strong gravitational lensing systems.

Several of the candidate systems were selected for the possibility of housing sources at multiple redshifts, key for our dark energy studies. While we do not endeavor in this work to perform detailed mass modeling of cluster-scale lenses with DES data, future higher-resolution imaging follow-up may allow for detailed modeling of cluster mass distributions.

[55] http://strides.physics.ucsb.edu/

The paper is organized as follows. In Section 2 we describe the DES SV season data. In Section 3 we present the lens search, followed by the spectroscopic follow-up in Section 4. We present the six confirmed systems and their properties in Section 5, discuss results in Section 6, and conclude in Section 7. All magnitudes are in the AB system. We assume a flat, Planck ΛCDM cosmology: $\Omega_M = 0.308$, $\Omega_\Lambda = 0.692$, and $H_0 = 67.8\ km\ s^{-1}\ Mpc^{-1}$ (Planck Collaboration et al. 2015).

2. DES SV DATA

The SV observing season took place from 2012 November 1 to 2013 February 23, immediately after the commissioning of the DECam (Flaugher et al. 2015). The survey started in 2013 August and has completed three seasons beyond SV. The survey and operations for SV and Year 1 are described in Diehl et al. (2014).

In total, SV observations cover ∼250 deg^2 in five optical filter bands (*grizY*), nearly reaching the expected full 5 yr depth of DES: below, we report median depth estimates of these data at 10σ galaxy limiting magnitude. The wide-field survey consists of the SPT-E and SPT-W fields that are located, respectively, in the east and west regions of the South Pole Telescope (SPT) survey footprint (Carlstrom et al. 2011): the *g*-band depth extends to ∼24.5 mag. The 30 deg^2 supernova survey takes place in eight shallow fields and two deep fields, extending to *g*-band depths, 25.0 and 25.4 mag, respectively.

The DES data management (DESDM) team was responsible for the reduction of the SV images. The basic reductions and coadd source detection were performed by DESDM (Desai et al. 2012; R. Gruendl 2015, in preparation): the software for reduction of SV exposures is similar to that used in the Y1A1 release.[56] The detrended, single-epoch images were calibrated, background-subtracted, and combined into "coadd tiles." Each coadd tile has dimensions $0.^\circ72 \times 0.^\circ72$, so defined as to cover the entire DES footprint. A catalog of objects was extracted from the coadded images using Source Extractor (SExtractor; Bertin & Arnouts 1996; Bertin 2011). Unless otherwise stated, photometric and position data of all objects in this work originate in this object catalog (see Table 1).

3. LENS SEARCH

The lens search, carried out by visually inspecting images, relied on morphology and color to identify lens candidates. We searched for arc- and ring-like features and multiply imaged sources, in association with red lensing galaxies or galaxy groups. Among the more typical of search criteria is the existence of blue source images in association with red galaxies, but some systems with red source images were also identified.

Although modern algorithms for automated arc- and ring-finders have improved in recent years, they still typically require manual intervention and/or subsequent visual inspection and verification (Lenzen et al. 2004; Horesh et al. 2005; Seidel & Bartelmann 2007; Marshall et al. 2009; More et al. 2012; Joseph et al. 2014). We performed a visual search without automated finders, because the SV sky area is relatively small and visual inspection is likely to recover the highest-ranking candidates that would be found with an automated finder. Given these search criteria, as well as the

[56] http://data.darkenergysurvey.org/aux/releasenotes/DESDMrelease.html

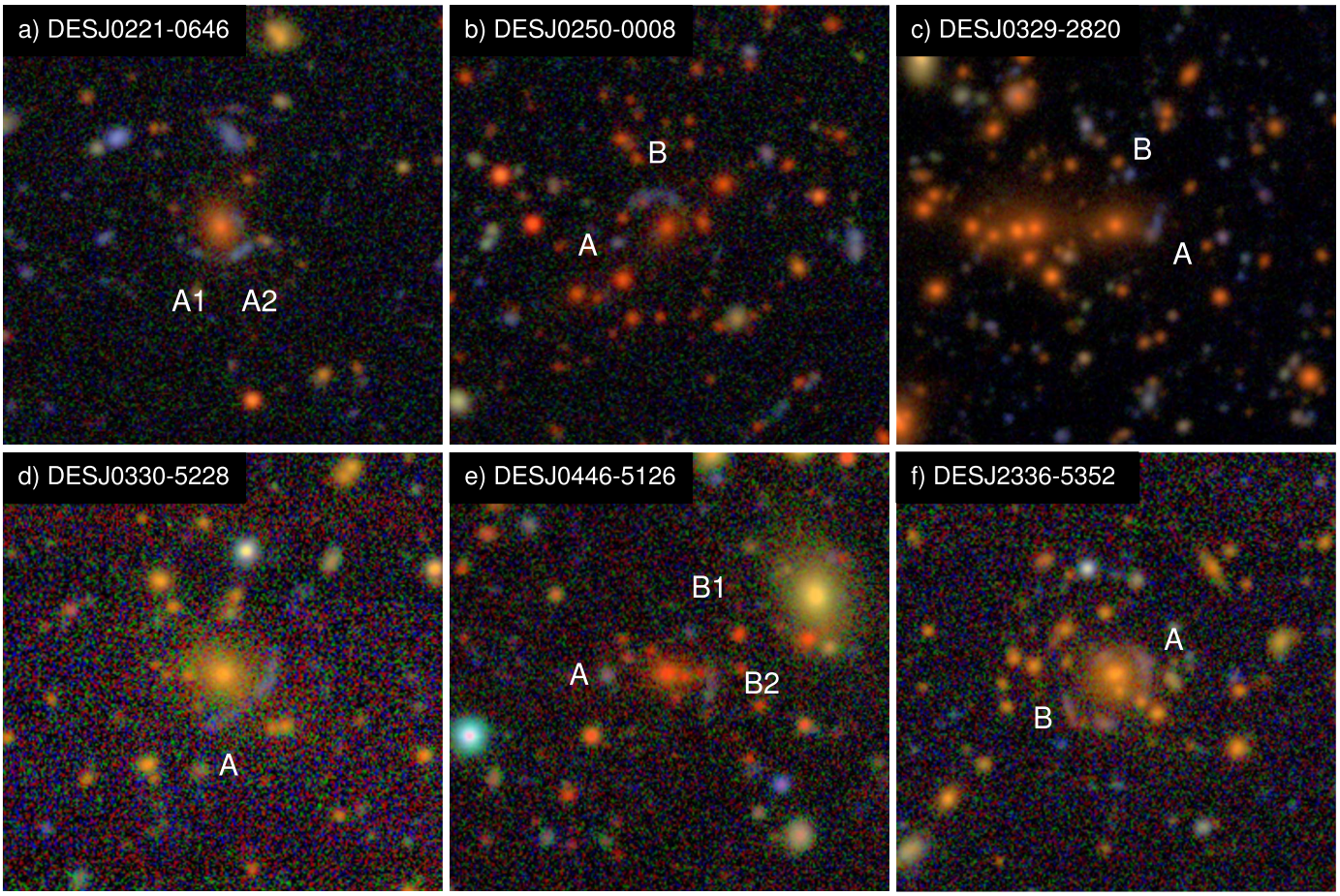

Figure 1. Color coadded DES images of the six systems described in this work: (a) DES J0221–0646, (b) DES J0250–0008, (c) DES J0329–2820, (d) DES J0330–5228, (e) DES J0446–5126, (f) DES J2336–5352. All images are oriented north up, east left, and are $1' \times 1'$ in area. The lensing features targeted for spectroscopy are indicated by the letters. Refer to Figures 2–7 for a more detailed view of the field and the image candidates.

pixel scale of DECam and the seeing of DES data, there is a bias toward larger Einstein radii, and thus higher mass (depending on the source redshift(s)), which are easier to identify through visual inspection.

We performed two types of visual scans. We performed a nontargeted search of all $\sim$250 deg^2—not focusing on any specific target regions or objects—as well as a targeted scan of previously identified galaxy clusters. The visual scan is performed on false-color PNG images, which are made by combining g, r, i coadd tiles (defined in Section 2) into color images.

The nontargeted search was carried out by about 20 inspectors, who systematically examined all the tiles. The open-area search yielded a sample of $\sim$1000 objects. Among the results of this search is the Cosmic Horseshoe (Belokurov et al. 2007), which was then removed from our sample of follow-up candidates.

We also carried out two targeted searches. The first one was carried out around the 67 known clusters from the SPT SZ survey (Bleem et al. 2015). Many of these clusters already have optical imaging follow-up and known lensing features. We identified nine candidates from this search. The second targeted search examined 374 galaxy clusters of richness >50, which themselves were found using the red-sequence Matched-filter Probabilistic Percolation cluster-finder algorithm (redMAPPer; Rykoff et al. 2014). This search yielded 39 candidates. The targeted search recovered known, confirmed lensing systems, such as BCS J2352–5452 (Buckley-Geer et al. 2011), RXC J2248.7–4431 (Böhringer et al. 2004), and ACT-CL J0102–4915 (El Gordo; Menanteau et al. 2012), which we then removed from the sample of candidates for spectroscopic follow-up.

The combined nontargeted and targeted search samples were merged and assessed by a team of experienced inspectors. Most of these objects were not convincing as strong lens system candidates or were not bright enough to expect successful spectroscopic follow-up. Each of the systems was assigned a rank, 1 to 3—with 1 signifying least likely to be a lens system, and 3 the most likely—on the basis of morphology, color, and brightness of sources. This ranking resulted in 53 promising ("rank 3") candidates.

To characterize the selection function of our sample, we compare to a sample of 87 high-quality candidates and confirmed lensing systems found in CFHTLS data. It includes a sample of 33 confirmed lenses from the RingFinder (Gavazzi et al. 2014), the 26 most promising candidates from ArcFinder as implemented in SL2S ARCS (SARCS; More et al. 2012), and 28 candidates from SpaceWarps (More et al. 2016), giving a total of 87 objects; the Einstein radii have a range of $1'' < \theta_E < 18''$. In the ArcFinder search, 12 candidates have giant arcs, which canonically have length-to-width ratio $\geqslant$8. CFHTLS has an effective search area of $\sim$150 deg^2 and depths of $g \sim 25.5$ and $\sim$26.5 mag in wide and deep fields, respectively.

Table 1
Properties of Lensing Systems: Positions and Photometry of Lenses and Source Images

System ID and Source Image ID	Object ID	R.A. (J2000) (deg)	Decl. (J2000) (deg)	(*g*, *r*, *i*, *z*, *Y*)
DES J0221–0646[a]	2937883420	35.463205	−6.792405	(23.32 ± 0.03, 21.79 ± 0.01, 20.73 ± 0.00, 20.25 ± 0.00)
A1	2937882680	35.464063	−6.793464	(24.38 ± 0.08, 24.07 ± 0.07, 23.88 ± 0.07, 23.62 ± 0.08)
A2	2937882790	35.46241	−6.793449	(23.49 ± 0.04, 23.18 ± 0.03, 22.87 ± 0.03, 22.70 ± 0.01)
DES J0250–0008	2925464779	42.534995	0.137950	(24.83 ± 0.18, 23.04 ± 0.18, 21.74 ± 0.02, 21.10 ± 0.01)
A	2925464554	42.537078	0.137222	(24.11 ± 0.10, 23.72 ± 0.06, 23.38 ± 0.07, 22.79 ± 0.04)
B	2925464667	42.534792	0.138905	(24.26 ± 0.11, 24.06 ± 0.08, 23.81 ± 0.10, 23.37 ± 0.08)
DES J0329–2820	2940549190	52.369631	−28.327630	(24.25 ± 0.03, 22.41 ± 0.01, 21.30 ± 0.00, 20.84 ± 0.00, 20.78 ± 0.06)
A	2940548768	52.367884	−28.327915	(24.39 ± 0.03, 23.96 ± 0.02, 23.41 ± 0.02, 23.13 ± 0.02, 22.85 ± 0.41)
B	2940548772	52.368948	−28.325491	(24.37 ± 0.03, 24.31 ± 0.03, 23.97 ± 0.03, 23.51 ± 0.02)
DES J0330–5228[b,c]	3081734463	52.737216	−52.470283	(22.04 ± 0.03, 20.10 ± 0.01, 19.33 ± 0.01, 18.91 ± 0.01, 18.74 ± 0.02)
A	3081733697	52.735917	−52.471431	(23.85 ± 0.14, 23.07 ± 0.09, 22.67 ± 0.13, 22.19 ± 0.13, 21.80 ± 0.31)
DES J0446–5126	2933341648	71.553645	−51.442376	(23.91 ± 0.05, 21.91 ± 0.01, 20.64 ± 0.01, 20.08 ± 0.01, 19.86 ± 0.02)
A	2933341522	71.557704	−51.442463	(23.24 ± 0.02, 22.64 ± 0.02, 22.33 ± 0.03, 22.11 ± 0.04, 22.28 ± 0.15)
B1	2933341657	71.552168	−51.440677	(24.47 ± 0.08, 23.80 ± 0.05, 23.59 ± 0.10, 23.52 ± 0.15, 23.70 ± 0.54)
B2	⋯	71.550762	−51.442894	(24.15 ± 0.07, 23.36 ± 0.05, 23.11 ± 0.04, 22.78 ± 0.04, 23.10 ± 0.23)
DES J2336–5352[d]	2968302040	354.029719	−53.876581	(22.41 ± 0.01, 20.48 ± 0.00, 19.57 ± 0.00, 19.20 ± 0.00, 19.21 ± 0.01)
A	2968302027	354.02782	−53.876292	(23.31 ± 0.02, 22.45 ± 0.02, 21.80 ± 0.02, 21.38 ± 0.02, 21.33 ± 0.05)
B	2968301854	354.032676	−53.878106	(24.18 ± 0.05, 23.33 ± 0.04, 22.47 ± 0.03, 22.14 ± 0.04, 22.20 ± 0.12)

Notes. Positions and photometry of objects for each confirmed strong-lensing system. Source Image ID refers to the arc or lensed source image discussed in the text, in Figure 1 and Figures 2–7. The Object ID is the unique identification number in the DESDM database of coadd objects. All positions (R.A., decl. in J2000) and magnitudes are drawn from the DESDM database, except in the case of source image B2 of DES J0446–5126: for this object, we measured aperture magnitudes via the Graphical Astronomy and Image Analysis software tool (GAIA 2015). *Y*-band photometry is provided where available: supernova fields were only observed in *Y*band for those fields that overlap with the wide-field survey, and arc B of DES J0329–2820 was too faint for detection in both DESDM and GAIA. Alternative identifications related to prior observations of some systems are listed as footnotes to this table.

[a] Object SA39: from More et al. (2012).

[b] SPT-CL J0330–5228/ACT-CL J0330–5227: from Bleem et al. (2015).

[c] Associated with radio source SUMSS J033057–522811 (Mauch et al. 2003; Werner et al. 2007).

[d] SCSO J233607–535235: from Menanteau et al. (2010a).

We estimate the lens-finding selection function of DES by counting the sources from the high-quality CFHTLS sample that survive a cut on the DES magnitude limit, which is taken to be 24.5 mag in *g*band for both the SV and full wide-field data. The source magnitudes of the samples listed above were provided by the author (A. More 2016, personal communication, 2015 November 11), and the calculation of the source magnitudes is discussed in Section 5.3 of More et al. (2016). After performing the magnitude cut, we linearly scaled the resulting counts by the ratio of the survey areas. From this comparison, we estimate that the full DES Wide-field survey will contain 2100 promising candidates. Scaling the area again for the DES SV area, we expect 105 promising candidates, which is nearly twice the amount found in the search discussed in this work.

A few factors likely contributed to the difference between the number of lens system candidates expected and discovered in DES SV data. The nontargeted search was performed by scanning large images, rather than cutouts around particular objects, as was done with the targeted search around clusters. In addition, some regions were only scanned once during the nontargeted search. Rigorous characterization of a strong lens candidate selection function requires the construction of a framework to measure each scanner's efficiency, completeness, and purity. Such a program was not implemented for the SV searches.

4. SPECTROSCOPIC FOLLOW-UP

We obtained spectroscopic follow-up observations with the Gemini Multi-object Spectrograph (GMOS; Hook et al. 2004) on the Gemini South Telescope, as part of the Gemini Large and Long Program GS-2014B-LP-5,[57] and with the Inamori-Magellan Areal Camera and Spectrograph (IMACS) multi-object spectrograph (Dressler et al. 2011) on the Magellan/Baade Telescope.

Of the 53 high-ranking candidates found during the lens search, we selected the 24 candidates most suitable for spectroscopic follow-up. For the purposes of planning the follow-up, the 24 candidates were ranked (1–3) by their surface brightness, which is calculated using a 2″-diameter aperture in the *i*band:

1. R1: $i_{\rm SB} < 23$ mag arcsec^{-2} (6 candidates);
2. R2: $23 < i_{\rm SB} < 24$ mag arcsec^{-2} (14 candidates);
3. R3: $i_{\rm SB} > 24$ mag arcsec^{-2} (4 candidates).

These rankings are not related to the quality rankings of candidates in Section 3. Details of the observing parameters and conditions for each of our confirmed lensing systems are shown in Table 2. We acquired spectroscopic follow-up for 21 of the 24 candidate systems: 17 systems were observed at Gemini and 5 at Magellan. One of the systems, DES

[57] http://www.gemini.edu/?q=node/12238#Buckley

Table 2
Spectroscopic Observation Log

DES System ID	UT Date	Telescope-Instrument	Grating	Total Integration (hr)	Seeing (arcsec)
DES J0221–0646	2014 Oct 10, 19	Gemini-GMOS	B600/R150	1/3.7	0.92/0.86
DES J0250–0008	2014 Oct 24	Gemini-GMOS	B600/R150	1/1	0.67/0.66
DES J0329–2820	2014 Oct 23	Magellan-IMACS	200 ℓ/nm	1	1.0
DES J0330–5228	2014 Oct 22	Gemini-GMOS	R150	1	0.71
DES J0446–5126	2014 Oct 19, 23	Gemini-GMOS	B600/R150	1/1.63	0.64/0.67
DES J2336–5352	2014 Oct 21	Gemini-GMOS	R150	1	0.73

Note. Observation log for follow-up spectroscopic observations. DES ID is derived from the R.A. and decl. position of the lensing object at the center of the system. For the Gemini observations, seeing is taken from the Gemini Observation Logs, which keep environmental conditions in 2 hr increments: the seeing for each exposure set is interpolated for the time of observation between adjacent recordings of the environmental log. For the Magellan observation, seeing is measured from the FWHM of the PSFs of the acquisition stars in the science exposures.

J0329–2820, was observed at both Gemini and Magellan: only B600 data were acquired at Gemini, which presented no spectral features, so we observed at longer wavelengths at Magellan.

We searched the Master Lens Database (L. Moustakas & J. Brownstein 2016, in preparation)[58] and the Gemini Science Archive[59] to ascertain whether any of our candidates had been previously discovered or confirmed. The Master Lens Database (last updated 2015 November 17) contains 657 candidates and confirmed systems. Out of these systems, 44 fall within our search area but were not identified as candidates for our follow-up program. They were identified by various programs, such as SL2S, SPT, and searches in GEMS and *HST* fields. About half of these candidates have estimated Einstein radii $\theta_{\rm E} < 2''$, and the maximum radius is $\sim 6''$; at least 80% are galaxy-scale lenses. Of the 44 candidates, the lensing features are barely visible or better in DES SV data for about one-third of the systems, but they are only obvious for a few. The limited resolution of the DES images obscures lensing features, especially for smaller-radius systems. Additionally, many features are faint and are not obviously lensing features, but could be chance projection or on-edge spirals, for example.

The only candidate that is in our confirmed sample is SA39 (More et al. 2012), discovered by the SL2S in CFHTLS data. We have obtained the first spectroscopic confirmation that SA39 is a strong-lensing system. This is DES J0221–0646 in our sample, and we present its confirmation in Section 5.1.

From the estimates of the selection function, we expect to find 105 promising candidates in DES, but we recovered 54. If all of the 44 missed candidates from the Master Lens Database are considered promising, then that would account for the discrepancy with our expectations described in Section 3. It is clear, however, that the image resolution is the principal factor in identification of systems with small Einstein radii.

4.1. Gemini/GMOS

We observed some of the lensing candidates at Gemini South using the multi-object mode on GMOS. The mask for each field was centered on the candidate lens of each system, and slits were placed on the candidate source images. In some cases, it was necessary to shift the field center to locate a suitable guide star. Accommodating as many source targets as possible sometimes required rotation of the slit mask (i.e., rotation of the position angle of each system). We placed slits on as many of the lensing features as possible, and the remaining ∼50 slits were placed on galaxy targets for photometric-redshift calibration of DES data. The slits were $1''$ in width and of varying length in order to accommodate both the object and an amount of sky sufficient to perform reliable background subtraction. In some cases, we tilted the slits to maximize the captured flux. We defined three sets of exposure times/grating combinations, which depend on the surface brightness classes defined above in Section 4:

1. R1: 1 hr integration with R150/GG455 grating/filter;
2. R2: 1 hr integration with B600 grating and 3.7 hr integration with R150/GG455 grating/filter;
3. R3: 1 hr integration with B600 grating.

We use the R150 grating in conjunction with the GG455 filter in order to obtain spectra with wavelength coverage ∼4500–10000 Å. For the sources that we expect to be late-type emission-line galaxies, this would allow us, in most cases, to detect [O II] λ3727 to $z \sim 1.7$, Hβ to $z \sim 1.0$, and Lyα in the range $z \sim 2.7$–7.2. We use the B600 grating to obtain spectral coverage of 3250–6250 Å, which would allow us to detect sources with $z > 2.0$ that emit Lyα.

A 1 hr observing sequence consisted of a pair of 900 s exposures, followed by a flat field taken with a quartz-halogen lamp and a calibration spectrum taken with a CuAr arc lamp. We then dithered to a different central wavelength to cover the gap between the CCDs and took a CuAr spectrum, followed by the flat-field exposure and then two more 900 s exposures. The 3.7 hr integration used the same sequence repeated 16 times, but with 840 s exposure times. Dividing the integration time into multiple exposures facilitates the removal of cosmic rays. The data were binned 2×2, giving effective dispersions of 0.1 and 0.386 nm/pixel for the B600 and R150 gratings, respectively. The low-surface-brightness systems (i.e., rank R3) underwent only 1 hr of integration with the B600 grating. The goal of this work is to confirm and further analyze a set of strong-lensing systems: to conserve telescope time and maximize the number of lensing system confirmations, we elected to not pursue longer integrations for a given candidate system, even if a clear spectroscopic signal did not appear. In addition, the photo-z calibration targets require observations with consistent depth, and thus integration time, across the observation fields.

[58] masterlens.astro.utah.edu
[59] http://www.cadc-ccda.hia-iha.nrc-cnrc.gc.ca/en/gsa/index.html

We used the Gemini IRAF package v2.16[60] to reduce all exposures. In each system, for each wavelength dither, we first process the flat field using the `gsflat` task (this includes subtraction of the bias). Each science exposure in a single dither is then reduced with `gsreduce` (using the previously processed flat fields), and then the two exposures are combined with `gemcombine`. Wavelength calibration and transformation are performed on each dither (using the `gswavelength` and `gstransform` tasks) before the pairs of dithers are coadded on a common wavelength scale to eliminate CCD chip gaps. We perform sky subtraction and one-dimensional (1D) spectral extraction using `gsextract`, which employs the `apall` task. Feature identification and redshift estimation are performed using the `emsao` task within the `rvsao` IRAF package (Kurtz & Mink 1998). We modified some of the Gemini IRAF tasks to provide more flexibility in the data reduction. In particular, we modified `gswavelength` and `gsextract` to allow one to perform 1D and two-dimensional (2D) fits on the calibration data and sky subtraction on the science data, respectively, for individual extensions.

Of the 21 observed candidate systems, 17 were observed at Gemini: 12 systems were observed in Priority Visiting observer mode from 2014 October 19 to 24, and five systems were observed in queue mode. For nine systems, we obtained all the planned exposures, and for eight systems, we obtained a subset of the planned exposures. The only planned 1 hr integrations acquired with the R150 grating (rank R1) were executed during the Priority Visiting Observer mode. The eight systems for which we did not obtain all planned exposures are missing the planned 3.7 hr R150 observations: in queue mode, these observations had lower Gemini observing priority. All planned 1 hr B600 observations were completed.

4.2. Magellan/IMACS

We also obtained spectra at Magellan with IMACS. The mask was again centered on the candidate lensing galaxy of each system. As with GMOS, we used 1″-width slits of varying length. We used the f/2 camera and the 200-ℓ/mm grism, because it has the best response in the redder wavelengths, and we used the WB5650-9200 filter to set the wavelength range to 5650-9200 Å. We took three 1200 s exposures for each mask to facilitate cosmic-ray removal. Two of the systems observed also had a 1 hr integration using the B600 grating using Gemini's GMOS. A ranking system was not used to select which systems to prioritize for observation.

To process the data, we used the COSMOS data reduction package.[61] This package performs wavelength calibration, followed by subtraction of bias, and division by flats, using the programs `Sflats` and `biasflat`. The sky is then subtracted using the program `subsky`. Finally, extraction of individual 1D or 2D spectral exposures is performed using `extract`, or `extract-2dspec`. Multiple sets of extracted spectra are then combined using `sumspec`. Feature identification and redshift estimation are performed using the `emsao` IRAF task.

Of the 21 observed candidate systems, 5 were observed on 2014 December 20–21 as part of a larger program to obtain spectroscopic redshifts of (1) supernova hosts and (2) galaxies for photometric redshift calibration of DES data. Note that one system, DES J0329–2820, was observed at both Magellan and Gemini.

[60] http://www.gemini.edu/sciops/data-and-results/processing-software
[61] http://code.obs.carnegiescience.edu/cosmos

5. CONFIRMED LENS SAMPLE

Of the 24 systems for which we sought follow-up, there was sufficient time to observe 21 systems. Of those, we confirmed a total of six strong-lensing systems. There are 15 systems that were observed but were not confirmed as lenses: nine have no discernible continuum emission (nor spectral features), four have continuum emission but no discernible features, and two were ruled out as lenses.

A number of the systems that we failed to confirm exhibit clear morphological and photometric lensing features. However, they would require significantly longer integration times or are located in the redshift desert—outside the range of the optical observations in our observing program. This highlights the challenge of obtaining spectra for the very faint objects found in deep optical surveys: a great deal of integration time, in tandem with IR spectrographs, may be required to confirm the large lens samples predicted in current and future large surveys. The candidates that were ruled out as lensing systems indeed exhibit suggestive morphological features, but the candidate lensed sources were determined to be foreground galaxies through spectroscopic analysis.

A multi-panel plot of the six confirmed systems is shown in Figure 1, and Table 1 lists the positions and photometry of the candidate lens and source(s) of each lensing system observed. The sample comprises one group-scale lens and five cluster-scale lenses. The group-scale lens DES J0221–0646 is known from the SARCS sample by SL2S (More et al. 2012), but had not been spectroscopically confirmed by that group. It was found during the nontargeted phase of our visual scan and later identified as a low-richness (<5) group in the redMAPPer catalog. Four lenses (DES J0250–0008, DES J0329–2820, DES J0446–5126, and DES J2336–5352) were also identified in the redMAPPer cluster-finder sample. DES J0330–5228 (SPT-CL J0330–5228/ACT-CL J0330–5227; Bleem et al. 2015) is a known candidate lensing systems from the SPT and Atacama Cosmology Telescope (ACT; Kosowsky 2006; Fowler et al. 2007) SZ surveys. DES J2336–5352 (SCSO J233607–535235; Menanteau et al. 2010a) is already known from the Southern Cosmology Survey (SCS; Menanteau et al. 2009). However, there were previously no spectroscopic observations of the lensing features in either of these systems. DES J0221–0646 and DES J0250–0008 were found in the slightly deeper DES supernova fields during the nontargeted searches.

In this section, we comment on each system, its spectral features of interest, and the derived redshifts. The reduced 1D spectra, alongside cutouts of the fields centered on the central lensing object showing the slit positions, targets, and Einstein radii, are shown for each system in Figures 2–7. Detailed algorithms do not yield mass model constraints that are signficantly better than enclosed masses (derived from Einstein radii) for systems that have a limited number of sources with multiple, detailed images.

Therefore, for each system, we employ a strategy similar to that of SBAS (e.g., Diehl et al. 2009) and estimate the enclosed mass $M_{\rm enc}$ of the lensing system, assuming a singular

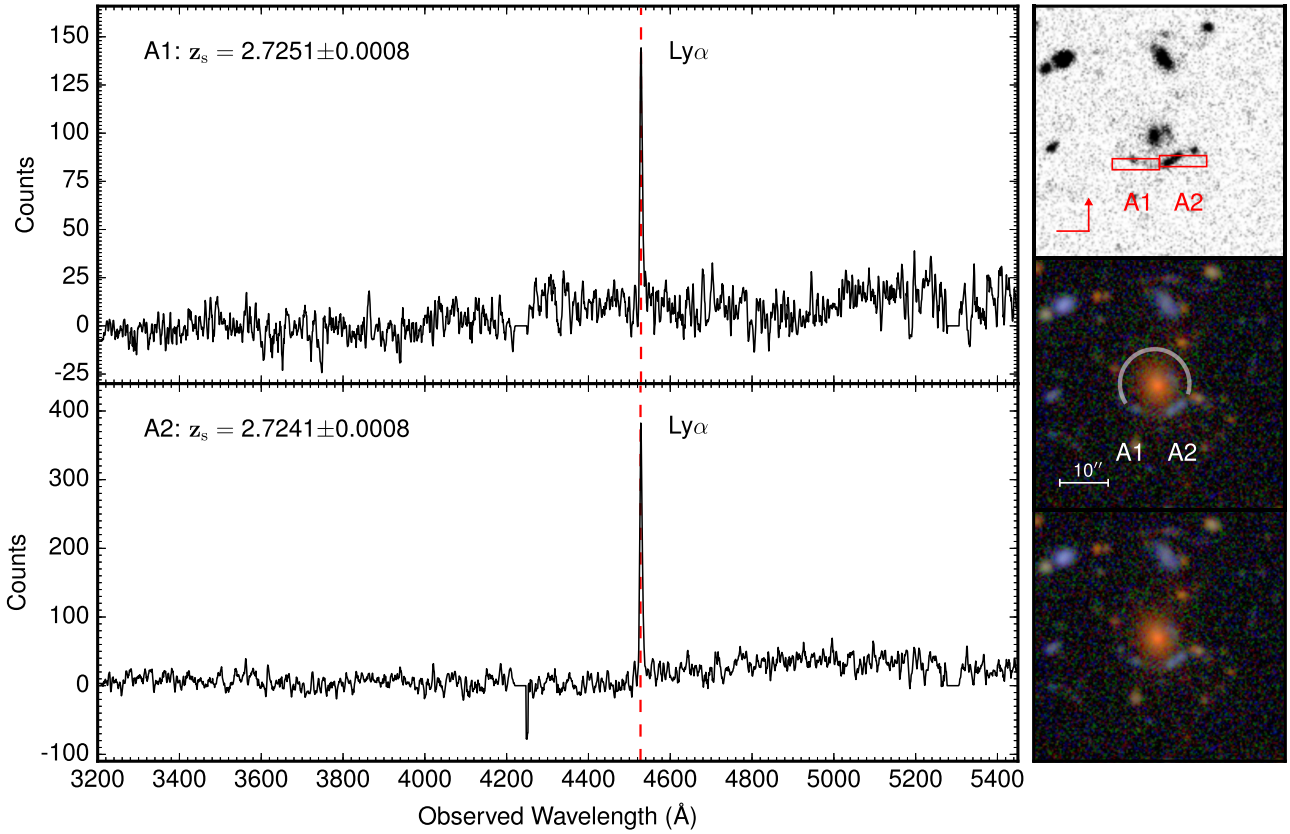

Figure 2. DES J0221–0646. The 1D spectra for A1 and A2 are shown on the left. There are strong emission lines at the same observed wavelength 4535 Å in both spectra. Taking into account the absence of other spectral features in the R150 spectra, along with the photometric redshift of the lens galaxy, we assign the features to be Lyα, which gives redshifts of $z_{\rm spec} = 2.7251 \pm 0.0008$ and 2.7241 ± 0.0008 for A1 and A2, respectively. The orientation of the slits (red boxes) is shown in the upper right DES *g*-band image. In the color coadd image in the middle right panel, the two features of interest are labeled "A1" and "A2," the Einstein radius is marked by a white arc, and the small scale bar shows the size of the image. In the lower right is an identical color coadd image. All images are oriented north up, east left. The flat, zero-count portions of the spectra near $\lambda \sim 4200$ and ~5300 Å show the chip gaps in the detectors: we did not take an offset observation to cover the chip gaps for this system.

isothermal sphere mass profile (Narayan & Bartelmann 1996):

$$M_{\rm enc} = \frac{c^2}{4G}\theta_{\rm E}^2\left(\frac{D_{\rm L}D_{\rm S}}{D_{\rm LS}}\right), \quad (1)$$

where c is the speed of light, G is Newton's gravitational constant, $\theta_{\rm E}$ is the Einstein radius, and D is the angular diameter distance. We estimate the Einstein radius (or radii if there is more than one source) by manually fitting a circle that passes through one or more spectroscopically confirmed features. The center is chosen to be the center of curvature of the candidate arc image(s). $D_{\rm L}$, $D_{\rm S}$, and $D_{\rm LS}$ are angular diameter distances to the lens, to the source, and between the lens and source, respectively: they depend only on the redshifts of these objects and on the cosmological parameters. The spectral features, photometric redshifts of lenses, spectroscopic redshifts of sources, Einstein radii, and enclosed masses are summarized in Table 3.

All of the confirmed systems are associated with redMAPPer groups or clusters. The cluster masses were measured with the procedure of Saro et al. (2015), which uses redMAPPer and SPT clusters to calibrate richness and mass. The spherical overdensity mass M_Δ is that enclosed within a radial boundary demarcated by a density contrast Δ with respect to the critical density. We summarize the redshifts, richnesses, and masses of these clusters in Table 3. The redMAPPer cluster redshifts are measured with the colors of all the cluster members, which affords a much smaller uncertainty in the cluster redshifts than that of the lensing galaxy for all systems. There are then likely to be some differences between the redshift of the single lensing galaxy and that of the cluster. However, except for the group-scale system, DES J0221–0646, the photometric redshift of the lensing galaxy and the redMAPPer-determined redshift agree within uncertainties—as they should, since the lensing galaxy is within the cluster.

We estimate frequentist uncertainties for the enclosed mass, which include uncertainties propagated from redshifts (via the angular diameter distances) and Einstein radii. The photometric redshift uncertainties have been multiplied by a factor of 1.5, according to the prescription of Sánchez et al. (2014) for photometric redshift measurements in DES. The spectroscopic redshift uncertainties are the result of a sum in quadrature of the wavelength calibration uncertainty and the redshift determination uncertainty from the IRAF function `emsao`.

The mass uncertainty is the sum in quadrature of the contributions from the Einstein radius and the three angular diameter distances. The uncertainty on each angular diameter distance scales with the redshift error, which varies from ~0.01% to ~5%, while uncertainty in the Einstein radius is at least ~15% among all systems. This disparity sets the Einstein radius as the dominant contributor to the uncertainty. In the manual fit, the uncertainty in the radius arises from variation of

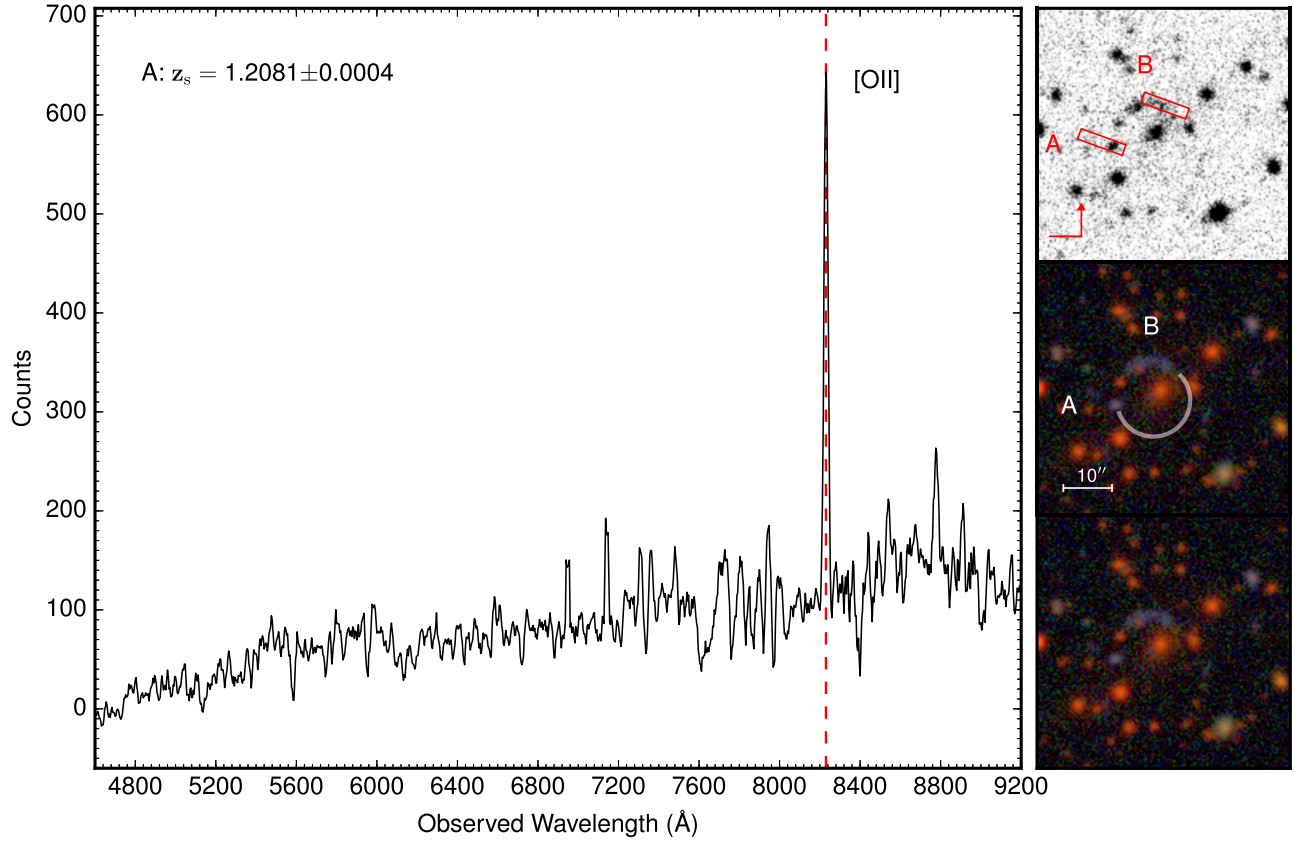

Figure 3. DES J0250–0008. The 1D spectrum for A is shown on the left. There is a strong emission line at an observed wavelength of 8229 Å. We associate this feature with [O II] λ3727, which yields a redshift of $z_{\rm spec} = 1.2081 \pm 0.0004$. The orientation of the slits (red boxes) is shown in the upper right DES *r*-band image. In the color coadd image in the middle right panel, the two features of interest are labeled "A" and "B," the Einstein radius is marked by a white arc, and small scale bar shows the size of the image. In the lower right is an identical color coadd image. All images are oriented north up, east left.

the arc's curvature over its extent, with the assumption that the correct center is chosen, as defined in Diehl et al. (2009). These uncertainties are estimated to be up to a few arcseconds. The distances between the source and lens cause some variation in the relative contributions to uncertainties: smaller distances provide for a greater contribution from the angular diameter distance $D_{\rm LS}$. This results in mass uncertainties in the range ~30%–80% (Table 3).

5.1. DES J0221–0646

DES J0221–0646 was originally discovered in CFHTLS (Object SA39; More et al. 2012) and encountered during our nontargeted search. It was also serendipitously found to be a group-scale lens in the redMAPPer catalog, with richness 4.64 ± 1.15 and redshift 0.603 ± 0.025. The central red galaxy of the lens has a DESDM photometric redshift of $z_{\rm lens} = 0.672 \pm 0.042$. There are two prominent blue arcs, A1 and A2, shown in Figure 1(a), to the southeast and southwest of the lensing galaxy, respectively. These arcs are also shown in the top and middle panels on the right of Figure 2. In the follow-up GMOS spectroscopy of both arcs, we identify strong emission lines (Figure 2, left panel) at the same observed wavelength (4535 Å) in both B600 spectra. Taking into account the absence of other spectral features in the R150 spectra, along with the photometric redshift of the lens galaxy, we assign the features to be Lyα, which gives redshifts of $z_{\rm spec} = 2.7251 \pm 0.0008$ and 2.7241 ± 0.0008 for arcs A1 and A2, respectively.

We estimate an Einstein radius of $\theta_{\rm E} = 6'' \pm 1''$, which passes through both arcs, giving an enclosed mass of $M_{\rm enc} = (1 \pm 0.4) \times 10^{13} M_{\odot}$.

In the DES imaging, there appear two arcs that may be counterimages. An arc north of arc A2, and extremely close to the lensing galaxy, may be a counterimage to arc A1. These objects appear more clearly in Figure 3, panel "39" of More et al. (2012). If we assume that arc A1 has a counterpart to the northeast, we can perform a manual measurement of the image-splitting distance: for lensing systems where the source lies nearly along the line of sight through the lens, the distance between an image and its counterimage is related to the Einstein radius, $\Delta\theta \sim 2\theta_{\rm E}$. For this system, $\Delta\theta = 8'' \pm 2''$, which gives $\theta_{\rm E} \sim 4'' \pm 2''$, in agreement with the direct manual measurement of the Einstein radius.

There is yet another possible counterimage slightly north and east of arc A1. These counterimages were not targeted: for a single multi-slit mask, it was not possible to obtain spectra for these objects simultaneously with that of the brighter arcs we had chosen (see top right panel of Figure 2 for the configuration of the mask slits).

5.2. DES J0250–0008

DES J0250–0008 is a newly discovered system identified in the redMAPPer cluster sample during the targeted search. The central red lensing galaxy has a photometric redshift of $z_{\rm lens} = 0.841 \pm 0.042$, with two blue features labeled A and B in Figures 1(b) and 3 (top and middle right panels); the arcs

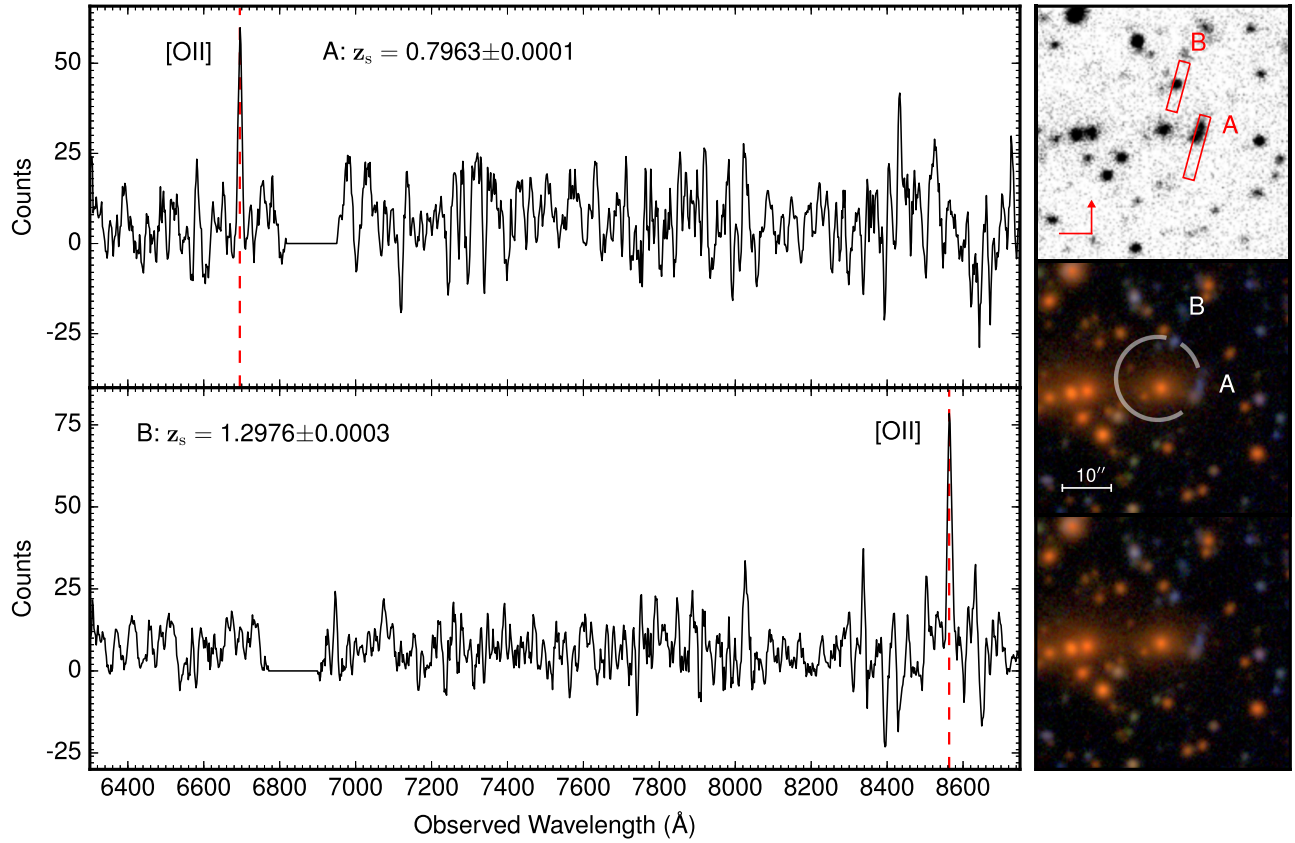

Figure 4. DES J0329–2820. The 1D spectra for A and B are shown on the left. There are emission lines at two different observed wavelengths, 6694 Å and 8563 Å. Given the lack of observed features at shorter wavelengths, we identify the emission as [O II] λ3727, from which we obtain redshifts $z_{\rm spec} = 0.7963 \pm 0.0001$ and 1.2976 ± 0.0003 for A and B, respectively. The orientation of the slits (red boxes) is shown in the upper right DES *g*-band image. In the color coadd image in the middle right panel, the two features of interest are labeled "A" and "B." The Einstein radii are marked by white and red arcs for slits A and B, respectively. The small scale bar shows the size of the image. In the lower right is an identical color coadd image. All images are oriented north up, east left. The flat, zero-count portions of the spectra near $\lambda \sim 6800$ Å show the chip gaps in the detectors: we did not take an offset observation to cover the chip gaps for this system.

are located east and north of the central cluster galaxy, respectively. We identify a strong emission line for A (Figure 3, left panel) in the GMOS R150 spectrum at an observed wavelength of 8229 Å. We associate this feature with [O II] λ3727, which yields a redshift of $z_{\rm spec} = 1.2081 \pm 0.0004$. We do not detect any continuum, nor any emission or absorption lines, from arc B.

While we do not detect features in the arc B spectrum, its morphology suggests that it is likely to be a lensed source image. Assuming that it is a feature of this system, we located the lensing mass center such that it aligns with the tangential arc B. As the circle of the Einstein radius passes through both images A and B, we use the spectroscopic redshift of arc A, and we estimate a single Einstein radius of $\theta_{\rm E} = 7'' \pm 2''$ for this system, which gives an enclosed mass of $M_{\rm enc} = (4 \pm 2) \times 10^{13} M_{\odot}$. The source of image A may lie outside the caustic and thus may not be strongly lensed, only weakly magnified. In such a case, this would provide a poor estimate of the enclosed mass.

5.3. DES J0329–2820

DES J0329–2820 is also a newly discovered system identified in the redMAPPer galaxy cluster sample during the targeted search. The central red galaxy has a photometric redshift $z_{\rm lens} = 0.655 \pm 0.033$. There are two small blue arcs, A and B, to the west and north of the central red galaxy in the image, shown in Figures 1(c) and 4, top and middle right panels. In the follow-up IMACS spectroscopy of the arcs, we identify emission lines at two different observed wavelengths of 6694 and 8563 Å. The GMOS B600 data for this system provide no observed features at shorter wavelengths; therefore, we identify the emission line as [O II] λ3727, from which we obtain redshifts $z_{\rm spec} = 0.7963 \pm 0.0001$ and 1.2976 ± 0.0003 for images A and B, respectively (Figure 4, left panel).

Arc B may be outside the caustic, and thus only weakly magnified and perhaps not multiply imaged. We therefore elect to use only A (the circle for which also goes through B). We then estimate a single Einstein radius of $\theta_{\rm E} = 7'' \pm 2''$ for A, which gives an enclosed mass of $M_{\rm enc} = (6 \pm 4) \times 10^{13} M_{\odot}$.

5.4. DES J0330–5228

DES J0330–5228 was discovered with *XMM-Newton*—via detection of a second X-ray peak (Werner et al. 2007)—as a cluster behind Abell 3128. It has also been measured in both the SPT (SPT-CL J0330–5228; Ruel et al. 2014) and ACT SZ surveys (ACT-CL J0330–5227; Menanteau et al. 2010b). The central red galaxy has a photometric redshift of $z_{\rm lens} = 0.463 \pm 0.046$. There is a very prominent blue arc (A) in Figure 1(d) to the southwest of the central lensing galaxy. In the follow-up GMOS R150 spectroscopy of the blue arc, we identify a strong emission line at an observed wavelength of 9146 Å, which we

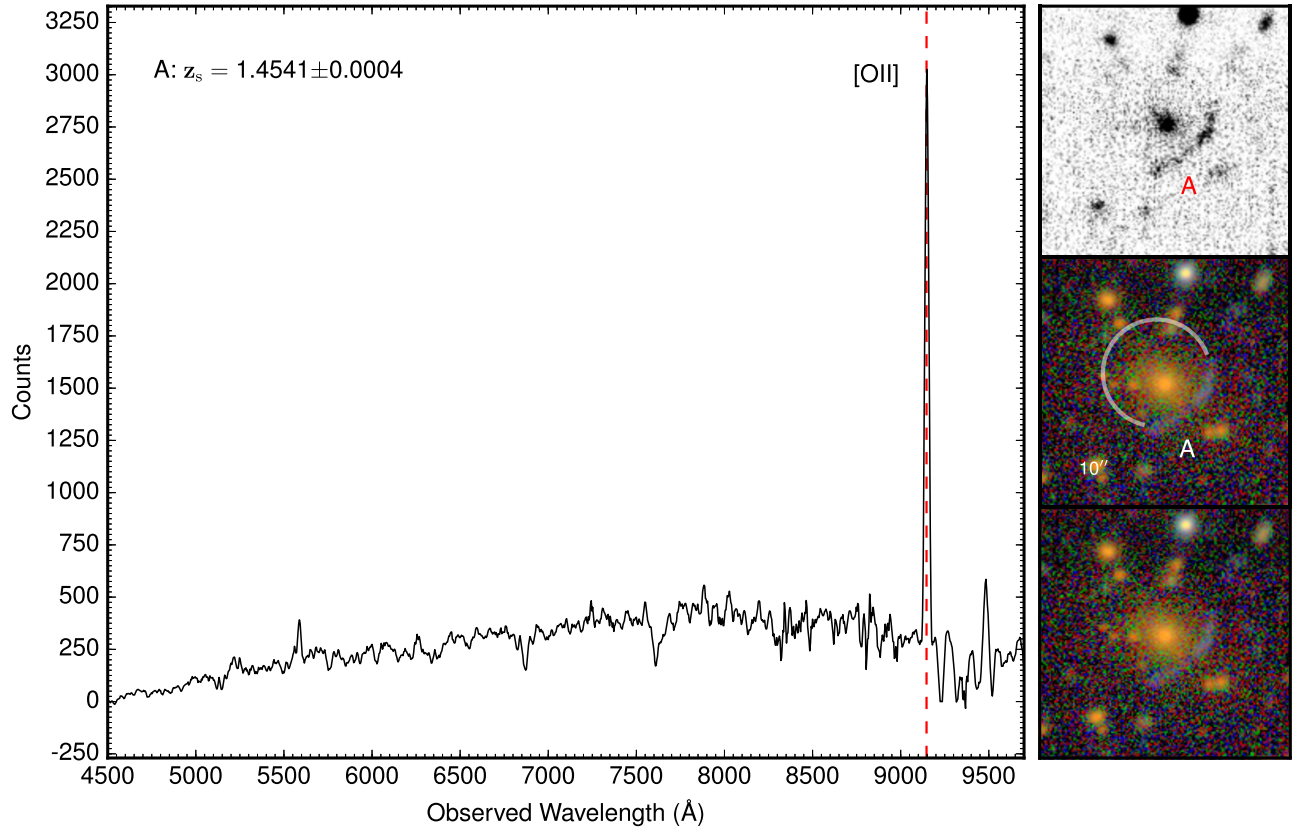

Figure 5. DES J0330–5228. The 1D spectrum for A is shown on the left. There is a strong emission line at an observed wavelength of 9146 Å, which we take to be [O II] λ3727, from which we obtain a redshift of $z_{\rm spec} = 1.4541 \pm 0.0004$. The orientation of the slit (red boxes) is shown in the upper right DES g-band image. In the color coadd image in the middle right panel, the feature of interest is labeled "A," the Einstein radius is marked by a white arc, and a small scale bar shows the size of the image. In the lower right is an identical color coadd image. All images are oriented north up, east left.

take to be [O II] λ3727, from which we obtain a redshift of $z_{\rm spec} = 1.4541 \pm 0.0004$ (Figure 5).

We placed the center to the northeast to coincide with the arc's curvature. We estimate an Einstein radius of $\theta_{\rm E} = 8'' \pm 2''$ for this system. Instead of the DES photometric redshift, we used the spectroscopic redshift from Werner et al. (2007), $z_{\rm spec} = 0.43961 \pm 0.00014$, to estimate an enclosed mass of $M_{\rm enc} = (2 \pm 0.8) \times 10^{13}\, M_{\odot}$. Werner et al. (2007) also estimate an Einstein radius of $\sim 6\farcs2$ and an upper limit on the mass of $\sim 5 \times 10^{12}\, M_{\odot}$; the authors noted that they only had a redshift measurement for the lens. Without a spectroscopic redshift for the source, the authors assumed a combined angular diameter distance of $D_{\rm L}\, D_{\rm S}/D_{\rm LS} = 1$ Gpc, which corresponds to an overestimate of the source redshift and thus an underestimate of the mass (see Equation (1)).

5.5. DES J0446–5126

DES J0446–5126 is also a newly discovered system, identified in the redMAPPer cluster-finder sample. Two small blue arcs, B1 and B2, lie to the northwest and southwest, respectively, of the central red galaxy; this is shown in Figure 1(e) and in the top and middle right panels of Figure 6. The candidate lensing galaxy has a photometric redshift of $z_{\rm lens} = 0.746 \pm 0.047$, in agreement with the redMAPPer cluster photometric redshift, $z_{\rm RM} = 0.734 \pm 0.020$.

The GMOS B600 spectroscopy reveals prominent emission lines (Figure 6, left panel) in both arcs at the same observed wavelength of 5117 Å. Given the appreciable strength of these emission lines in the B600 spectra, we expected to see other strong lines, such as Hβ in the R150 spectrum. However, additional features did not appear, and we therefore concluded that this emission line is Lyα, from which we obtain spectroscopic redshifts of $z_{\rm spec} = 3.2068 \pm 0.0010$ and 3.2086 ± 0.0011 for B1 and B2, respectively. The object labeled A in Figure 1(e) also has emission lines (not shown), which we interpret as [O II] λ3727 and [O III] λ5007. This gives a redshift of $z_{\rm spec} = 0.1680 \pm 0.0009$, making object A a foreground object.

We estimate an Einstein radius of $\theta_{\rm E} = 7'' \pm 2''$ for this system, which gives an enclosed mass of $M_{\rm enc} = (2 \pm 0.9) \times 10^{13} M_{\odot}$.

5.6. DES J2336–5352

DES J2336–5352 is a galaxy cluster originally found in the SCS, and it has a cluster photometric redshift of $z_{\rm c} = 0.54$ (SCSO J233607–535235; Menanteau et al. 2010a). It is also found in the redMAPPer cluster-finder sample, which gives a photometric redshift $z_{\rm RM} = 0.522 \pm 0.011$, in agreement with the DES photometric redshift, $z_{\rm lens} = 0.530 \pm 0.075$.

There are two small red arcs, A and B, to the west and southeast of the central red galaxy, respectively. These are shown in Figure 1(f) and in the top and middle right panels of Figure 7. The GMOS R150 spectra of these two arcs show prominent emission lines at two different observed wavelengths—8023 Å for A and 7070 Å for B—which we identify as [O II] λ3727. These yield source redshifts of

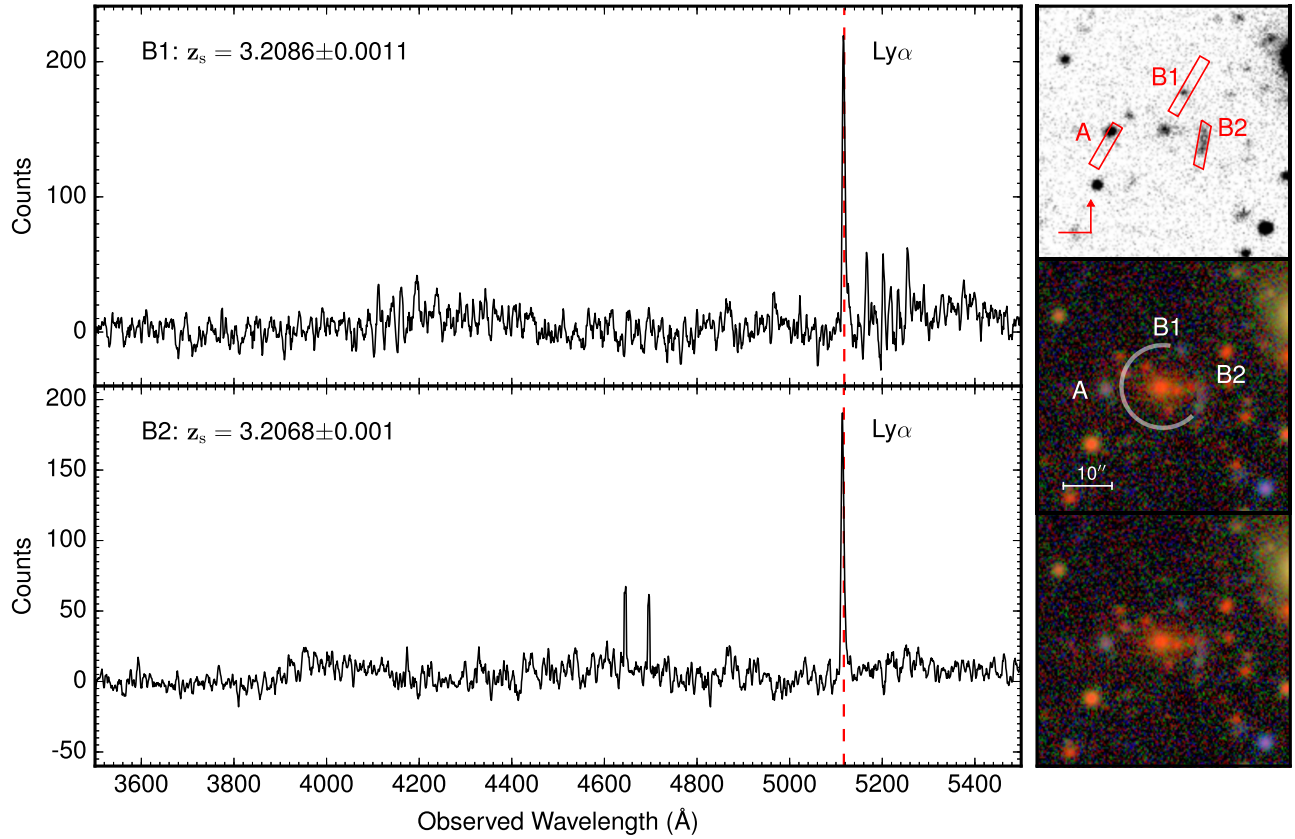

Figure 6. DES J0446–5126. The 1D spectra for B1 and B2 are shown on the left. The spectrum for A is not shown, but has an emission line consistent with an interpretation as a foreground object. There are prominent emission lines in both arcs at the same observed wavelength of 5117 Å. We conclude that this is Lyα emission, from which we obtain redshifts of $z_{\rm spec} = 3.2068 \pm 0.0010$ for B and 3.2086 ± 0.0011 for C. The object labeled A also has emission lines (not shown), which we interpret as [O II] λ3727 and [O III] λ5007. This gives a redshift of $z_{\rm spec} = 0.1680 \pm 0.0009$, making object A a foreground object. The orientation of the slits (red boxes) is shown in the upper right DES g-band image. In the color coadd image in the middle right panel the three features of interest are labeled "A," "B1," and "B2," the Einstein radius is marked by a white arc, and the small scale bar shows the size of the image. In the lower right is an identical color coadd image. All images are oriented north up, east left.

$z_{\rm spec} = 1.1528 \pm 0.0006$ and 0.8972 ± 0.0004 for A and B, respectively (Figure 7, left panel).

We estimate an Einstein radius of $\theta_{\rm E} = 5'' \pm 2''$ for A and $\theta_{\rm E} = 9'' \pm 2''$ for B, which give enclosed masses of $M_{\rm enc} = (9 \pm 7) \times 10^{12} M_{\odot}$ and $M_{\rm enc} = (4 \pm 2) \times 10^{13} M_{\odot}$, respectively.

We note that normally one would expect the lower-redshift source to have a smaller $\theta_{\rm E}$ than the higher-redshift one, but that does not seem to be the case here. Arc B may be outside the caustic, and thus only weakly magnified and not multiply imaged; it is also not clearly tangentially aligned with the candidate lens, which makes it less likely to be a lensed source.

There also exists a faint image to the west of arc B, almost directly south of the central red lensing galaxy, that may be another source or counterimage. To provide sufficient sky coverage in the slit for arc B, this image could not also be observed in a single mask.

6. DISCUSSION

Many of our unconfirmed systems exhibit clear lensing features but have no detectable continuum or spectral features, with integration times of about 1 hr on an 8 m class telescope.[62] The need for long integration time highlights the challenge of obtaining spectra for faint objects found by deep optical surveys, like DES: the challenge will only be greater for the Large Synoptic Survey Telescope[63] (LSST; LSST Science Collaboration et al. 2009). One faces the prospect of long integration times, which limits the number of systems that can be followed up with a typical program. For systems that exhibit a clear lensing morphology and that have detectable continuum emission but no visible features, IR data may be necessary to confirm them.

A number of large telescopes housing UV to infrared spectroscopic instruments are planned for the coming 10–20 yr, which will help to alleviate this pressure. The Thirty Meter Telescope[64] will require a mere hour of integration on $i \sim 25$ for low-noise spectroscopic measurements—similarly for the Giant Magellan Telescope.[65] However, with their expected high subscription rate, it remains to be seen whether there will be enough time to follow up the systems predicted for projects like LSST.

While Gemini's GMOS instrument covers optical wavelengths in multi-slit or long-slit mode, the Very Large Telescope's X-shooter[66] provides long-slit capability for strong-lens follow-up simultaneously in optical and near-IR

[62] For a number of the targets, we did not obtain the 3.7 hr GMOS R150 observations, which might have helped to confirm more systems.

[63] http://www.lsst.org/lsst/
[64] http://ast.noao.edu/system/us-tmt-liaison/survey-faq
[65] http://www.gmto.org/
[66] https://www.eso.org/sci/facilities/paranal/instruments/xshooter.html

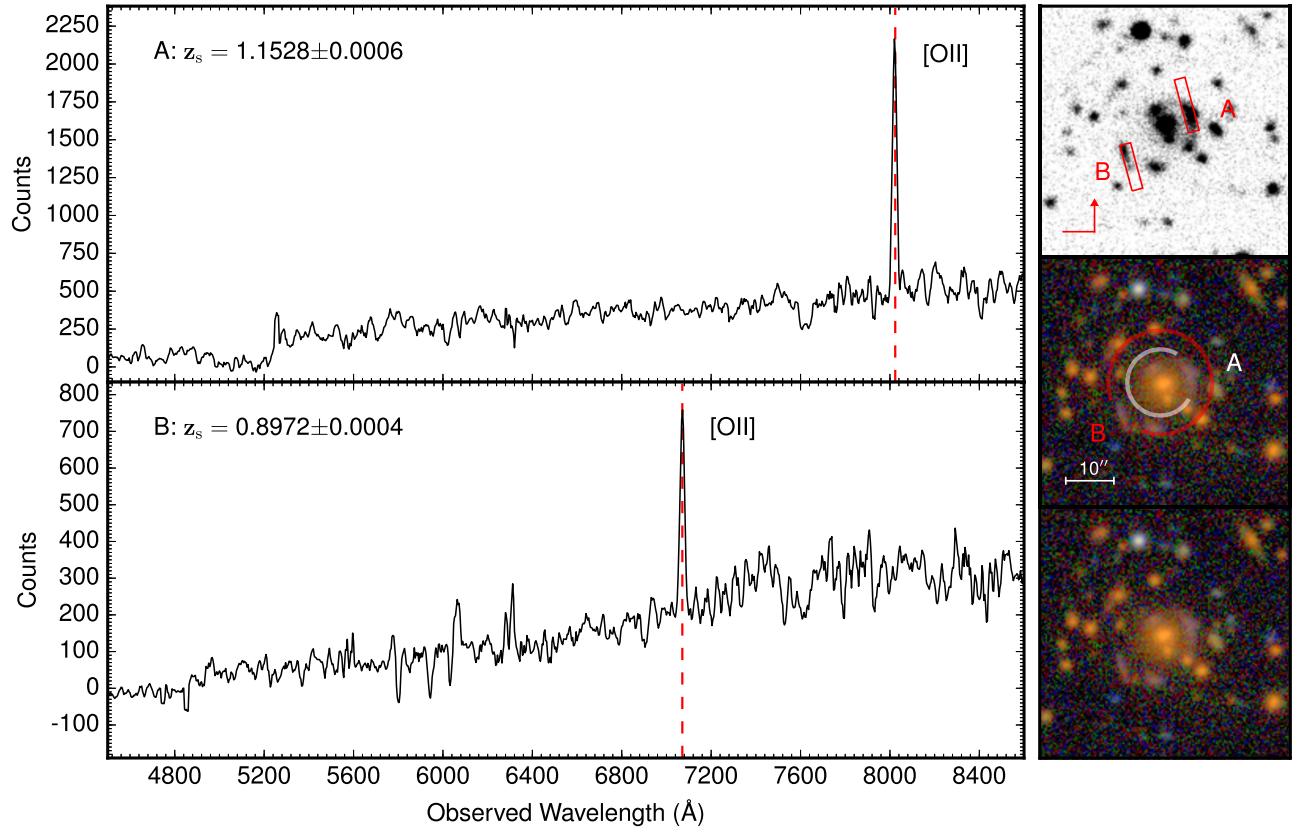

Figure 7. DES J2336–5352. The 1D spectra for A and B are shown on the left. The prominent emission lines at two different observed wavelengths of 8023 Å for A and 7070 Å for B are due to [O II] λ3727. These lines yield source spectroscopic redshifts of $z_{spec} = 1.1528 \pm 0.0006$ and 0.8972 ± 0.0004 for A and B, respectively. The orientation of the slits (red boxes) is shown in the upper right DES *g*-band image. In the color coadd image in the middle right panel the two features of interest are labeled "A" and "B." The Einstein radii are marked by white and red arcs for slits A and B, respectively. The small scale bar shows the size of the image. In the lower right is an identical color coadd image. All images are oriented north up, east left.

wavelengths. X-shooter is the first second-generation instrument on the 8 m VLT: it has an echelle spectrograph that (1) covers a spectral range 300–2500 nm at intermediate resolution ($R \sim 4{,}000$–$17{,}000$) and (2) operates in long-slit or IFU mode (Vernet et al. 2011). In addition, new instruments are being proposed for the Gemini Observatories via the Gemini Instrument Feasibility study.[67] For example, the Gemini Multi-Obect eXtra-wide-band Spectrograph (GMOX; Robberto et al. 2015) has a three-arm spectrograph covering the entire optical and near-IR spectrum that is available from the ground. Another example, OCTOCAM, is a multi-channel imager and long-slit spectrograph, also covering the optical and near-IR wavelengths (de Ugarte Postigo 2015). Both GMOX and OCTOCAM add integral field capability, which are ideal for extended lenses. If integration times are sufficiently low for these new instruments, the Gemini observatories may provide a competitive resource for follow-up of lensing systems in future surveys.

7. SUMMARY

In this paper we presented the first confirmed group- and cluster-scale strong-lensing systems found in DES data. These systems were discovered through visual identification using both targeted and nontargeted searches. We confirmed these systems with a combination of spectroscopy from GMOS on the Gemini South telescope and IMACS on the Magellan/Baade telescope.

Two of these systems are of particular interest because they have source galaxies at redshifts $z = 2.7251$ and $z = 3.22086$. Due to the magnification provided by lensing, these sources are typically among the brightest galaxies in their redshift ranges and can provide an important window into the star formation history and galaxy formation at these cosmic epochs.

The candidate lensing systems discovered in DES SV data span a range of arc sizes, much like the currently known sample of candidates from searches during the past decade. Due to the seeing limitations of DES (median expected seeing $\sim 0\farcs9$), systems with smaller arc separations were more difficult to identify, especially during the nontargeted search. Thus, our visual inspection methods likely yielded higher completeness in the targeted search of redMAPPer and SPT clusters.

As we examine more of the DES wide-field area, we expect to find many more systems. Through comparison with the CFHTLS data, we expect there to be ~2100 lenses in the full survey, which is similar to the number found in the preceding decade of survey searches in optical and IR wavelengths listed in Section 1. Independently, Collett (2015) predicts 800 galaxy-scale lenses.

The Year 1 DES data cover an area of ~1800 deg^2, and we have already conducted targeted searches, identifying a number of promising systems for follow-up. We have also expanded the search techniques to use arc-finding (e.g., More et al. 2012) and ring-finding algorithms (e.g., Gavazzi et al. 2014), as well

[67] https://www.gemini.edu/node/12362

Table 3
Lensing Features

System ID and Source ID (Spec. Feat.)	Lens Redshift $z_{\rm lens}$	Spec. Redshift $z_{\rm spec}$	Einstein Radius $\theta_{\rm E}$ (arcsec)	Enclosed Mass $M_{\rm enc}$ ($M_\odot$)	redMAPPer Mass $M_{500,\rm RM}$ ($M_\odot$)	redMAPPer Richness	redMAPPer Redshift $z_{\rm RM}$
DES J0221–0646	0.672 ± 0.042	…	…	…	$<.67 \times 10^{14}$	4.6 ± 1.2	0.603 ± 0.025
A1 (Lyα)	…	2.7251 ± 0.0008	6 ± 1	$1 \pm 0.4 \times 10^{13}$	…	…	…
A2 (Lyα)	…	2.7241 ± 0.0008	…	…	…	…	…
DES J0250–0008	0.841 ± 0.042	…	…	…	$3.72 \pm 0.71 \times 10^{14}$	64.6 ± 6.0	0.841 ± 0.013
A ([O II]3727)	…	1.2081 ± 0.0004	7 ± 2	$4 \pm 2 \times 10^{13}$	…	…	…
B (none)	…	…	…	…	…	…	…
DES J0329–2820	0.655 ± 0.033	…	…	…	$3.58 \pm 0.69 \times 10^{14}$	57.7 ± 3.4	0.671 ± 0.016
A ([O II]3727)	…	0.7963 ± 0.0001	7 ± 2	$6 \pm 4 \times 10^{13}$	…	…	…
B ([O II]3727)	…	1.2976 ± 0.0003	…	…	…	…	…
DES J0330–5228	0.463 ± 0.046	0.43961 ± 0.00014	…	…	$7.19 \pm 1.26 \times 10^{14}$	114.5 ± 11.4	0.435 ± 0.013
A ([O II]3727)	…	1.4541 ± 0.0004	8 ± 2	$2 \pm 0.8 \times 10^{13}$	…	…	…
DES J0446–5126	0.746 ± 0.047	…	…	…	$2.84 \pm 0.58 \times 10^{14}$	41.9 ± 5.0	0.730 ± 0.030
A ([O II]3727/[OIII]5007)	…	0.1680 ± 0.0009	…	…	…	…	…
B1 (Lyα)	…	3.2068 ± 0.0010	7 ± 2	$2 \pm 0.9 \times 10^{13}$	…	…	…
B2 (Lyα)	…	3.2086 ± 0.0011	…	…	…	…	…
DES J2336–5352	0.530 ± 0.075	…	…	…	$6.84 \pm 1.21 \times 10^{14}$	92.7 ± 5.0	0.521 ± 0.010
A ([O II]3727)	…	1.1528 ± 0.0006	5 ± 2	$9 \pm 7 \times 10^{12}$	…	…	…
B ([O II]3727)	…	0.8972 ± 0.0004	9 ± 2	$4 \pm 2 \times 10^{13}$	…	…	…

Note. Lensing features of confirmed systems and properties of associated redMAPPer clusters. In the left section, we show the DESDM object IDs for lenses (as in Table 1), the source image IDs, and the emission lines identified in the source spectra. In the middle section, we show the photometric redshifts of lenses $z_{\rm lens}$, spectroscopic redshifts $z_{\rm spec}$, Einstein radii $\theta_{\rm E}$, and derived enclosed masses $M_{\rm enc}$. Ellipsis points indicate features that were not measured. For all of the systems, photometric redshifts (drawn from the the DESDM database) were obtained for the lensing galaxies. The uncertainties have been multiplied by 1.5 times the original estimate, according to the results of Sánchez et al. (2014) for estimating uncertainties in DES photometric redshift measurement codes. The photometric redshifts of the sources within the DESDM database were not found to be reliable when compared with the spectroscopic redshift measurements made in this work: the source redshifts are too large for accurate photometric estimations. Redshifts for the sources are those measured from spectroscopic follow-up at Gemini South and Magellan; please see Section 4 for details of the spectroscopic follow-up. Only one lensing galaxy has a spectroscopic redshift: in DES J0330–5228, we used that measured by Werner et al. (2007). For five of the six systems, morphology indicates a single Einstein radius and enclosed mass for a given system. For each of the systems DES J0221–0646 and DES J0446–5126, we measured a single Einstein radius that intersects two images with the same source redshift. DES J0250–0008 and DES J0330–5228 each have only one source image with redshifts. DES J0329–2820 has two source redshifts, but only one is chosen for the radius measurement. In DES J2336–5352, the lower-redshift source has, anomalously, a larger radius; arc B may be outside the caustic and thus only weakly magnified and not multiply imaged. Please see Sections 5.1–5.6 for details of the analysis in each system. In the rightmost section, we show the properties of the associated redMAPPer clusters. The masses are measured with the methods of Saro et al. (2015). The mass calibration method does not reach to low enough masses and richness to provide a complete probability distribution for the mass of this DES J0221–0646; we instead cite an upper limit. The redMAPPer redshifts are measured for the entire cluster with the colors of all the cluster members, which affords a much smaller uncertainty in the redMAPPer redshifts than that of the lensing galaxy for all systems.

as catalog-based photometry searches similar to those employed in the SBAS (e.g., Diehl et al. 2009). We continue the dedicated program, STRIDES (Treu et al. 2015), to search for lensed quasars. With these tools, our searches through Year 1 data will be more effective than in SV for finding galaxy-scale lenses. The high yields of DES and future surveys will likely pose a challenge for spectroscopic follow-up and thus a challenge to maximize strong lensing for use in constraining cosmology.

We are grateful for the extraordinary contributions of our CTIO colleagues and the DES Camera, Commissioning, and Science Verification teams for achieving excellent instrument and telescope conditions that have made this work possible. The success of this project also relies critically on the expertise and dedication of the DES Data Management organization.

Funding for the DES Projects has been provided by the U.S. Department of Energy, the U.S. National Science Foundation, the Ministry of Science and Education of Spain, the Science and Technology Facilities Council of the United Kingdom, the Higher Education Funding Council for England, the National Center for Supercomputing Applications at the University of Illinois at Urbana-Champaign, the Kavli Institute of Cosmological Physics at the University of Chicago, the Center for Cosmology and Astro-Particle Physics at the Ohio State University, the Mitchell Institute for Fundamental Physics and Astronomy at Texas A&M University, Financiadora de Estudos e Projetos, Fundação Carlos Chagas Filho de Amparo à Pesquisa do Estado do Rio de Janeiro, Conselho Nacional de Desenvolvimento Cientfico e Tecnológico and the Ministério da Ciência e Tecnologia, the Deutsche Forschungsgemeinschaft, and the Collaborating Institutions in the Dark Energy Survey. The DES data management system is supported by the National Science Foundation under Grant Number AST-1138766. The DES participants from Spanish institutions are partially supported by MINECO under grants AYA2012-39559, ESP2013-48274, FPA2013-47986, and Centro de Excelencia Severo Ochoa SEV-2012-0234, some of which include ERDF funds from the European Union.

The Collaborating Institutions are Argonne National Laboratory, the University of California at Santa Cruz, the University of Cambridge, Centro de Investigaciones Energéticas, Medioambientales y Tecnológicas-Madrid, the University of Chicago, University College London, the DES-Brazil Consortium, the Eidgenoessische Technische Hochschule (ETH) Zurich, Fermi National Accelerator Laboratory, the University of Edinburgh, the University of Illinois at Urbana-Champaign, the Institut de Ciències de l'Espai (IEEC/CSIC), the Institut de Física d'Altes Energies, Lawrence Berkeley National Laboratory, the Ludwig-Maximilians Universität and the associated Excellence Cluster Universe, the University of Michigan, the National Optical Astronomy Observatory, the University of Nottingham, the Ohio State University, the University of Pennsylvania, the University of Portsmouth, SLAC National Accelerator Laboratory, Stanford University, the University of Sussex, and Texas A&M University.

We are also grateful to Janani Sivakumar, student at the Illinois Mathematics and Science Academy, as well as Caroline Odden and her students, Kathryn Chapman, George Avecillas, and Matthew Simon, at the Phillips Academy, for their contributions to the scanning effort. We also thank Matthew Becker and Risa Wechsler for helpful discussions on the topic of galaxy cluster richnesses and masses.

This work is based in part on observations obtained at the Gemini Observatory, which is operated by the Association of Universities for Research in Astronomy, Inc., under a cooperative agreement with the NSF on behalf of the Gemini partnership: the National Science Foundation (United States), the National Research Council (Canada), CONICYT (Chile), the Australian Research Council (Australia), Ministério da Ciência, Tecnologia e Inovação (Brazil), and Ministerio de Ciencia, Tecnología e Innovación Productiva (Argentina). The data were acquired through the Gemini Science Archive and processed using the Gemini IRAF package v2.16.

Thanks to the entire Las Campanas Observatory staff for their help in the acquisition of the Magellan/IMACS data (IMACS; Bigelow & Dressler 2003). This paper includes data gathered with the 6.5 m Magellan Telescopes located at Las Campanas Observatory, Chile.

C.F. acknowledges funding from CAPES (proc. 12203-1). This paper has gone through internal review by the DES collaboration. This research has made use of NASA's Astrophysics Data System.

C.D.B. would like to thank CNPq for the financial support.

R.J.F. gratefully acknowledges support from the Alfred P. Sloan Foundation.

Fermilab is operated by Fermi Research Alliance, LLC, under Contract No. DE-AC02-07CH11359 with the United States Department of Energy.

REFERENCES

Agnello, A., Treu, T., Ostrovski, F., et al. 2015, MNRAS, 454, 1260
Allam, S. S., Tucker, D. L., Lin, H., et al. 2007, ApJL, 662, L51
ALMA Partnership, Vlahakis, C., Hunter, T. R., et al. 2015, ApJL, 808, L4
Belokurov, V., Evans, N. W., Hewett, P. C., et al. 2009, MNRAS, 392, 104
Belokurov, V., Evans, N. W., Moiseev, A., et al. 2007, ApJL, 671, L9
Bertin, E. 2011, in ASP Conf. Ser. 442, Astronomical Data Analysis Software and Systems, ed. I. N. Evans et al. (San Francisco, CA: ASP), 435
Bertin, E., & Arnouts, S. 1996, A&AS, 117, 393
Bigelow, B. C., & Dressler, A. M. 2003, Proc. SPIE, 4841, 1727
Birrer, S., Amara, A., & Refregier, A. 2015, arXiv:1511.03662
Blain, A. W. 1996, MNRAS, 283, 1340
Bleem, L. E., Stalder, B., de Haan, T., et al. 2015, ApJS, 216, 27
Böhringer, H., Schuecker, P., Guzzo, L., et al. 2004, A&A, 425, 367
Bolton, A. S., Burles, S., Koopmans, L. V. E., et al. 2008, ApJ, 682, 964
Browne, I. W. A., Wilkinson, P. N., Jackson, N. J. F., et al. 2003, MNRAS, 341, 13
Buckley-Geer, E. J., Lin, H., Drabek, E. R., et al. 2011, ApJ, 742, 48
Bussmann, R. S., Pérez-Fournon, I., Amber, S., et al. 2013, ApJ, 779, 25
Cabanac, R. A., Alard, C., Dantel-Fort, M., et al. 2007, A&A, 461, 813
Carlstrom, J. E., Ade, P. A. R., Aird, K. A., et al. 2011, PASP, 123, 568
Collett, T. E. 2015, ApJ, 811, 20
Collett, T. E., & Auger, M. W. 2014, MNRAS, 443, 969
Collett, T. E., Auger, M. W., Belokurov, V., Marshall, P. J., & Hall, A. C. 2012, MNRAS, 424, 2864
de Ugarte Postigo, A. 2015, IAUGA, 22, 57336
Desai, S., Armstrong, R., Mohr, J. J., et al. 2012, ApJ, 757, 83
Diehl, H. T., Abbott, T. M. C., Annis, J., et al. 2014, The Dark Energy Survey and Operations: Year 1, doi:10.1117/12.2056982
Diehl, H. T., Allam, S. S., Annis, J., et al. 2009, ApJ, 707, 686
Dressler, A., Bigelow, B., Hare, T., et al. 2011, PASP, 123, 288
Egami, E., Rex, M., Rawle, T. D., et al. 2010, A&A, 518, L12
Fassnacht, C. D., Blandford, R. D., Cohen, J. G., et al. 1999, AJ, 117, 658
Faure, C., Kneib, J.-P., Covone, G., et al. 2008, ApJS, 176, 19
Flaugher, B., Diehl, H. T., Honscheid, K., et al. 2015, arXiv:1504.02900
Fowler, J. W., Niemack, M. D., Dicker, S. R., et al. 2007, ApOpt, 46, 3444
GAIA 2015, Graphical Astronomy and Image Analysis Tool, http://star-www.dur.ac.uk/~pdraper/gaia/gaia.html
Gavazzi, R., Marshall, P. J., Treu, T., & Sonnenfeld, A. 2014, ApJ, 785, 144
Gavazzi, R., Treu, T., Koopmans, L. V. E., et al. 2008, ApJ, 677, 1046

Hennawi, J. F., Gladders, M. D., Oguri, M., et al. 2008, AJ, 135, 664
Hook, I. M., Jørgensen, I., Allington-Smith, J. R., et al. 2004, PASP, 116, 425
Horesh, A., Ofek, E. O., Maoz, D., et al. 2005, ApJ, 633, 768
Jackson, N. 2008, MNRAS, 389, 1311
Joseph, R., Courbin, F., Metcalf, R. B., et al. 2014, A&A, 566, A63
Jullo, E., Natarajan, P., Kneib, J.-P., et al. 2010, Sci, 329, 924
Kosowsky, A. 2006, 50, 969
Kubik, D. 2007, Master's thesis, Northern Illinois Univ.
Kubo, J. M., Allam, S. S., Annis, J., et al. 2009, ApJL, 696, L61
Kubo, J. M., Allam, S. S., Drabek, E., et al. 2010, ApJL, 724, L137
Kurtz, M. J., & Mink, D. J. 1998, PASP, 110, 934
Lenzen, F., Schindler, S., & Scherzer, O. 2004, A&A, 416, 391
Lin, H., Buckley-Geer, E., Allam, S. S., et al. 2009, ApJ, 699, 1242
LSST Science Collaboration, Abell, P. A., Allison, J., et al. 2009, arXiv:0912.0201
Marshall, P. J., Hogg, D. W., Moustakas, L. A., et al. 2009, ApJ, 694, 924
Mauch, T., Murphy, T., Buttery, H. J., et al. 2003, MNRAS, 342, 1117
McKean, J. P., Browne, I. W. A., Jackson, N. J., et al. 2005, MNRAS, 356, 1009
Menanteau, F., Hughes, J. P., Jimenez, R., et al. 2009, ApJ, 698, 1221
Menanteau, F., Hughes, J. P., Barrientos, L. F., et al. 2010a, ApJS, 191, 340
Menanteau, F., González, J., Juin, J.-B., et al. 2010b, ApJ, 723, 1523
Menanteau, F., Hughes, J. P., Sifón, C., et al. 2012, ApJ, 748, 7
More, A., Verma, A., Marshall, P. J., et al. 2016, MNRAS, 455, 1191
More, A., Cabanac, R., More, S., et al. 2012, ApJ, 749, 38
Myers, S. T., Jackson, N. J., Browne, I. W. A., et al. 2003, MNRAS, 341, 1
Narayan, R., & Bartelmann, M. 1996, arXiv:astro-ph/9606001
Negrello, M., Perrotta, F., González-Nuevo, J., et al. 2007, MNRAS, 377, 1557
Negrello, M., Hopwood, R., De Zotti, G., et al. 2010, Sci, 330, 800
Oguri, M., & Marshall, P. J. 2010, MNRAS, 405, 2579
Planck Collaboration, Ade, P. A. R., Aghanim, N., et al. 2015, arXiv:1502.01589
Reblinsky, K., & Bartelmann, M. 1999, A&A, 345, 1
Refsdal, S. 1964, MNRAS, 128, 307
Robberto, M., Heckman, T., Gennaro, M., et al. 2015, IAUGA, 22, 57947
Ruel, J., Bazin, G., Bayliss, M., et al. 2014, ApJ, 792, 45
Rykoff, E. S., Rozo, E., Busha, M. T., et al. 2014, ApJ, 785, 104
Sánchez, C., Carrasco Kind, M., Lin, H., et al. 2014, MNRAS, 445, 1482
Saro, A., Bocquet, S., Rozo, E., et al. 2015, MNRAS, 454, 2305
Seidel, G., & Bartelmann, M. 2007, A&A, 472, 341
Smail, I., Ivison, R. J., & Blain, A. W. 1997, ApJL, 490, L5
Suyu, S. H., Auger, M. W., Hilbert, S., et al. 2013, ApJ, 766, 70
Swinbank, A. M., Smail, I., Chapman, S. C., et al. 2010, MNRAS, 405, 234
Treu, T. 2010, ARA&A, 48, 87
Treu, T., Agnello, A. & Strides Team 2015, in American Astronomical Society Meeting Abstracts 225, #318.04
Vernet, J., Dekker, H., D'Odorico, S., et al. 2011, A&A, 536, A105
Vieira, J. D., Crawford, T. M., Switzer, E. R., et al. 2010, ApJ, 719, 763
Vieira, J. D., Marrone, D. P., Chapman, S. C., et al. 2013, Nature, 495, 344
Werner, N., Churazov, E., Finoguenov, A., et al. 2007, A&A, 474, 707
Wiesner, M. P., Lin, H., Allam, S. S., et al. 2012, ApJ, 761, 1
Willis, J. P., Hewett, P. C., Warren, S. J., Dye, S., & Maddox, N. 2006, MNRAS, 369, 1521
York, D. G., Adelman, J., Anderson, J. E., Jr., et al. 2000, AJ, 120, 1579
York, T., Jackson, N., Browne, I. W. A., et al. 2005, MNRAS, 361, 259